Simulated Geophysical Noise in Sea Ice Concentration Estimates of Open Water and Snow-Covered Sea Ice

Rasmus T. Tonboe, Vishnu Nandan, Marko Mäkynen, *Member, IEEE*, Leif Toudal Pedersen, Stefan Kern, Thomas Lavergne, Johanne Ølund, Gorm Dybkjær, Roberto Saldo, and Marcus Huntemann

***Abstract*—Sea ice concentration algorithms using brightness temperatures (T_B) from satellite microwave radiometers are used to compute sea ice concentration (c_{ice}), sea ice extent, and generate sea ice climate data records. Therefore, it is important to minimize the sensitivity of c_{ice} estimates to geophysical noise caused by snow/sea ice thermal microwave emission signature variations, and presence of WV and clouds in the atmosphere and/or near-surface winds. In this study, we investigate the effect of geophysical noise leading to systematic c_{ice} biases and affecting c_{ice} standard deviations (STD) using simulated top of the atmosphere T_Bs over open water and 100% sea ice. We consider three case studies for the Arctic and the Antarctic and eight different c_{ice} algorithms, representing different families of algorithms based on the selection of channels and methodologies. Our simulations show that, over open water and low c_{ice}, algorithms using gradients between V-polarized 19-GHz and 37-GHz T_Bs show the lowest sensitivity to the geophysical noise, while the algorithms exclusively using near-90-GHz channels have by far the highest sensitivity. Over sea ice, the atmosphere plays a much smaller role than over open water, and the c_{ice} STD for all algorithms is smaller than over open water. The hybrid and low-frequency (6 GHz) algorithms have the lowest sensitivity to noise over sea ice, while the polarization type of algorithms has the highest noise levels.**

***Index Terms*—Microwave radiometry, sea ice concentration, sea ice emission modeling.**

I. Introduction

SATELLITE microwave brightness temperatures (T_B) measured at atmospheric window frequencies and used for estimating sea ice concentration (c_{ice}) are sensitive to noise from the atmosphere and variability in surface emissivity and temperature, here referred to as geophysical noise [1]. This geophysical T_B sensitivity varies with electromagnetic frequency and polarization. Although, in general, the sensitivity to geophysical noise is minimized in c_{ice} algorithms, the estimated c_{ice} may still inherit sensitivity of the T_Bs to these geophysical noise sources, and its influence on c_{ice} can be systematic, as a bias, or high frequency in time and space, quantified as a standard deviation. Over open water (OW), the T_Bs are sensitive to wind roughening of the water surface, total columnar water vapor (WV) in the atmosphere, and cloud liquid water (CLW) [2]. Over sea ice, the atmospheric emission and extinction is small (dryer atmosphere than over OW), compared to the high emission from the sea ice background, except at near-90 GHz, where the T_Bs are sensitive to WV and CLW also over ice [3]. The T_B variability from sea ice is dominated by variability caused by scattering, reflection, and emission processes at or beneath the snow surface, as well as by the snow/sea ice volume internal temperature profile [36], [39]. Over sea ice, we distinguish between surface and atmospheric noise.

An earlier investigation of different c_{ice} algorithms by Tonboe and Andersen [35] used measured snow and ice geophysical properties as input to an emission model and perturbed the snow density and snow grain size of specific layers in the snow pack. They showed that the T_B gradient algorithms had a low sensitivity to these changes, while the algorithms using near-90-GHz channels had a high sensitivity to the snow surface density.

In the marginal ice zone, the atmospheric extinction may be high affecting the T_Bs, and thus, also the c_{ice} estimates. In fact, different algorithms with different sensitivity to the atmospheric extinction and surface emission demonstrate diverse trends in sea ice area and extent over seasonal- and decadal-time scales, using the same T_B input [4]. This means that, not only does the sea ice area have a climatic trend, but the noise sources are also affecting the T_Bs and c_{ice} systematically and are changing with, e.g., the wind patterns, WV, and CLW amounts in the atmosphere [2].

Some processing facilities, e.g., EUMETSAT's OSISAF (Ocean and Sea Ice Satellite Application Facility) use explicit correction of the measured T_Bs before computing c_{ice} ([1], [37], [22]). This is a spatiotemporal varying noise reduction

Manuscript received August 16, 2021; revised October 29, 2021; accepted December 2, 2021. Date of publication December 9, 2021; date of current version January 31, 2022. This work was supported by the European Space Agency's European Earth Watch Programme, Global Monitoring of Essential Climate Variables (GMECV), under contract 4000126449/19/I-NB. *(Corresponding author: Rasmus T. Tonboe.)*

Rasmus T. Tonboe, Leif Toudal Pedersen, and Roberto Saldo are with the Technical University of Denmark, 2800 Lyngby, Denmark (e-mail: rtt@space.dtu.dk; ltp@space.dtu.dk; rs@space.dtu.dk).

Vishnu Nandan is with the University of Manitoba, Winnipeg, MB R3T 2N2, Canada (e-mail: vishnu.nandan@umanitoba.ca).

Marko Mäkynen is with the Finnish Meteorological Institute, FI-00101 Helsinki, Finland (e-mail: marko.makynen@fmi.fi).

Stefan Kern is with the University of Hamburg, 20144 Hamburg, Germany (e-mail: stefan.kern@uni-hamburg.de).

Thomas Lavergne is with the Norwegian Meteorological Institute, Oslo 0313, Norway (e-mail: thomas.lavergne@met.no).

Johanne Ølund and Gorm Dybkjær are with the Danish Meteorological Institute, Kobenhavn 2100, Denmark (e-mail: joe@dmi.dk; gd@dmi.dk).

Marcus Huntemann is with the University of Bremen, 28359 Bremen, Germany (e-mail: marcus.huntemann@uni-bremen.de).

Digital Object Identifier 10.1109/JSTARS.2021.3134021

method over both ice and OW. The correction uses numerical weather prediction (NWP) model data (10-m wind, 2-m air temperature, surface temperature, WV) and a parametrized atmospheric radiative transfer model (RTM) to correct T_Bs [41]. The success of the noise reduction depends on the quality of the NWP data and on the used RTM. In addition, the procedure applies adjustment of the tie-points to avoid potential biases from the NWP data and the RTM. These are called dynamical tie-points and they are typical signatures of sea ice and OW which are used in the c_{ice} algorithms.

A lot of effort has already been invested in processing c_{ice} climate data records (CDRs), where the sensitivity to noise has been minimized regionally using auxiliary data and RTMs for the T_B correction and using hemispherical dynamical tie-points [37], [22]. However, it is not currently possible to correct for all atmospheric noise sources. For example, the temporal and spatial resolution and the quality of CLW in NWP forecasts and reanalyses are not adequate for correction of T_B [15], [24]. Also, the parameters in the snow and ice are difficult to measure or quantify in numerical models and they have not yet been used for explicit correction. When computing sea ice CDRs, it is therefore important to find algorithms with low sensitivity to the physical parameters which are difficult to correct for. This includes CLW and snow and ice parameters in general. It is common practice to combine algorithms with a low sensitivity to noise over sea ice with those with a low sensitivity to noise over OW into hybrid algorithms so an algorithm does not have to perform everywhere [13], [22]. We are interested in the identification of variables in the snow/sea ice system, for example, snow depth (Hs) and snow ice interface temperature (T_{si}) which are central for the T_B and c_{ice} variability.

This study is part of a c_{ice} algorithm evaluation development in the European Space Agency (ESA) Climate Change Initiative (CCI) sea ice project [14]. The project is developing capacity to construct a sea ice CDR from satellite data, including sea ice thickness from radar altimetry (ERS 1-2, ENVISAT, Cryosat-2, and Sentinel - 3) and c_{ice}, area, and extent from microwave radiometer data [15], [22]. Here, we focus entirely on CDR applications and the estimated c_{ice} sensitivity to the geophysical noise in following three cases. Two sites were selected in the Antarctic: One in the Ross Sea (75°S, 200°E) representing 100% first-year sea ice (FYI) and one in the Bellingshausen Sea (64°S, 280°E) representing OW. One site was selected in the Arctic in the Lincoln Sea (85°N, 240°E) representing 100% multiyear sea ice (MYI). We have selected only two sea ice cases to be able to analyze individual snow precipitation events. The Ross Sea simulation is typical for the Antarctic with a relatively thick snow cover on FYI and the Lincoln Sea simulation is typical for Arctic MYI. The Bellingshausen Sea open water simulation is representative for atmospheric conditions and sea state near the ice edge.

We want to identify algorithms and noise sources leading to systematic biases in the c_{ice}. This has two purposes: 1) to avoid c_{ice} biases and ensure CDR stability, and 2) to identify noise sources that could potentially be corrected for. In this study, we do not consider intermediate c_{ice}, i.e., concentrations in between 0% and 100% and summer sea ice melt conditions specifically.

The rest of this article is organized as follows. First, we present the thermodynamic and emission models and the sea ice concentration algorithms in Section II. Next, we present the results for the three different cases (FYI, MYI, OW) in Section III, and end with discussion and conclusions in Section IV.

II. Thermodynamic Sea Ice Model and Its Interface to Sea Ice Emission Model and Sea Ice Concentration Algorithms

The flowchart in Fig. 1 shows the procedure in our study: 1) The multilayer sea ice model described in Ref. [39] takes the initial snow/ice profiles in Tables I and II and meteorological reanalysis data as input and simulates snow and sea ice profiles at very high vertical resolution at every time step; 2) the sea ice emission model described in Ref. [26] ingests those profiles and computes the sea ice self-emission brightness temperature and emissivity; 3) the atmospheric emission over ice and the OW T_B is simulated using the atmospheric/ocean emission model, which is a modified version of [41] here called WM2000; and, finally, 4) the simulated T_Bs are input to eight different sea ice concentration algorithms for computing c_{ice}.

The snow and sea ice thermodynamical model and its interface to the sea ice emission model are described in Refs. [39], [36]. The same methodology has also been used for studying other applications, e.g., sea ice emissivity [39], sea ice temperature [36], and applied in forward model development [38].

We aim to identify the role and impact of individual noise sources over OW and on snow-covered sea ice at the top of the atmosphere (TOA) T_B, and at the sea ice surface T_B to separate the contributions from the surface and the atmosphere. Therefore, a one-dimensional multilayer snow/ice thermodynamic model has been developed to provide realistic ranges of microphysical input to a sea ice emission model. The emission model is then simulating T_Bs which are input to eight sea ice concentration algorithms, as shown in Fig. 1.

The c_{ice} noise is understood as variability around a reference, where the "true" reference is exactly 0% or 100% c_{ice}, respectively. The dataset that we use is simulated using either a combined thermodynamic model for sea ice forced with reanalysis meteorological data [40] and a microwave emission model over sea ice, or a microwave emission model forced with reanalysis meteorological data over OW (see Fig. 1).

A. Multilayer Sea Ice Model

In microwave emission modeling for sea ice applications, parameters such as temperature, density, snow grain size, and ice salinity at centimeter-scale vertical resolution are needed, in addition to snow depth and ice thickness. The thermodynamic model is forced with ECMWF ERA40 data [40] input at 6-h intervals: Surface air pressure (P), 2-m air temperature (Ta), and dew point temperature converted to relative humidity (rh), 10-m wind speed (Ws), down-welling shortwave (Sw), long-wave radiation (Lw), and six-hourly accumulated precipitation (Mr), total column water (TCW), total column WV, and the difference between the two is the CLW. As the snow and sea ice thermal conductivity is a function of temperature, the model uses an

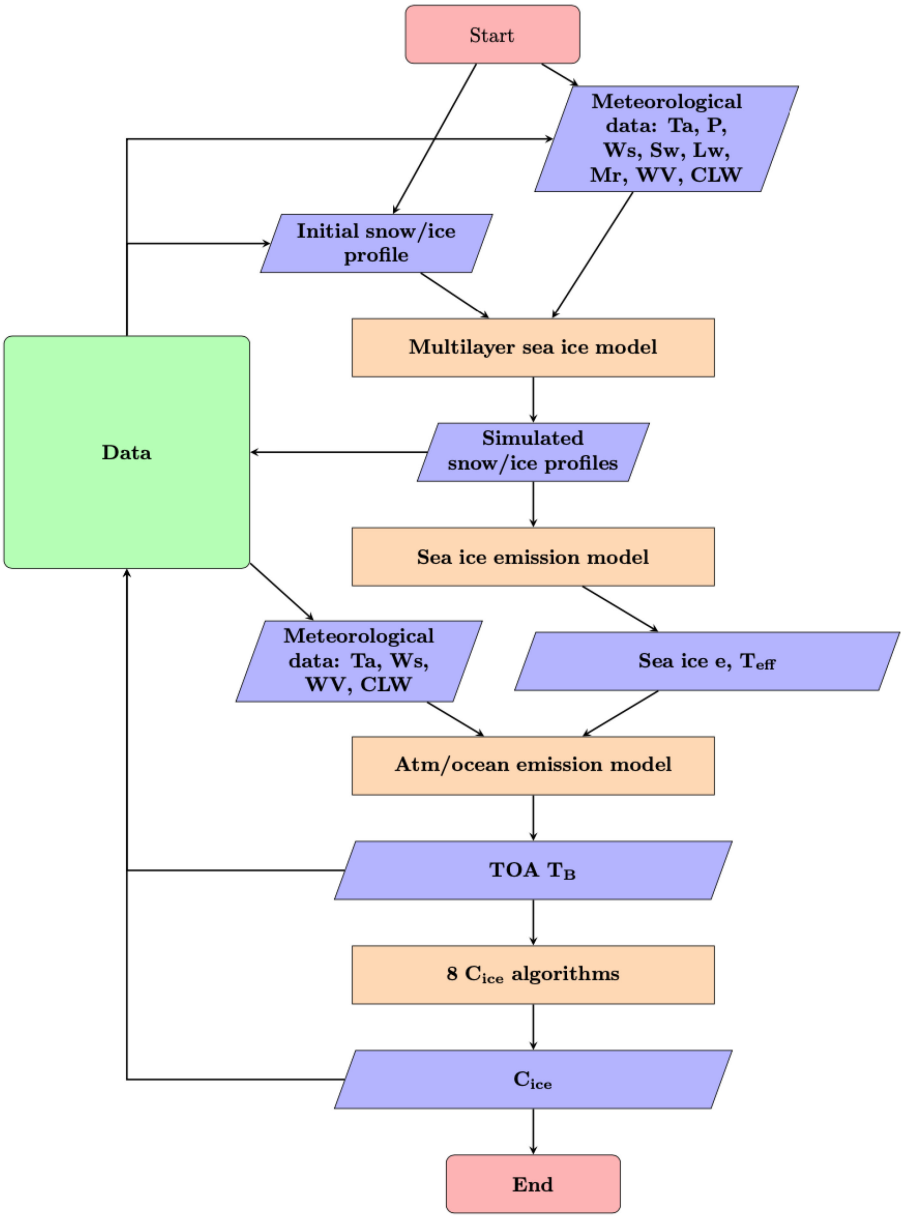

Fig. 1. Flowchart showing the sequence of models and input/output data. The models and the input/output data are also summarized in Table III and the initial snow/ice profiles are shown in Table I for FYI and Table II for MYI. Red boxes in the flowchart are the start and end of the process, blue boxes indicate the input/output data, and orange boxes indicate a process. The green "Data" box is where all input/output data are stored for later analysis. The arrows point in the direction of the data flow.

TABLE I
INITIAL 1.5 CM FIRST-YEAR ICE PROFILE INPUT TO THE EMISSION MODEL AT THE BEGINNING OF FREEZE-UP (THE BEGINNING OF THE SIMULATION)

Layer	Temperature [K]	Density [kg/m^3]	layer thickness [m]	Correlation length [mm]	Salinity [ppt]	Type
1	269	920	0.01	0.20	22.0	sea ice
2	270	920	0.005	0.20	8.0	sea ice

iterative procedure between each 6-h time step except for the snow precipitation which is released at the beginning of each time-step.

The thermodynamic model has the following prognostic parameters for each layer: Thermometric temperature (K), density (kg/m^3), thickness (m), snow grain size (m), type (new snow, recrystalized, or old snow, FYI, MYI), ice salinity (ppt), and snow liquid water content (m^3/m^3) (we only used simulations while the temperature is below the freezing point of water and snow liquid water content is therefore 0). Snow layering is very important for the microwave signatures; therefore, the model treats snow layers related to individual snow precipitation events,

TABLE II
INITIAL MULTIYEAR ICE PROFILE INPUT TO THE EMISSION MODEL AT THE BEGINNING OF THE SIMULATION. LAYER 4 IS SUBDIVIDED INTO 49 LAYERS EACH 0.05-M THICK TO RESOLVE THE TEMPERATURE PROFILE

Layer	Temperature [K]	Density $[kg/m^3]$	Layer thickness [m]	Correlation length [mm]	Salinity $[ppt]$	Type
1	270	300	0.05	0.35	0.00	old snow
2	270	900	0.05	1.25	0.50	sea ice
3	270	900	0.15	0.85-0.35	1.00	sea ice
4	270	910	2.25	0.25	2.50	sea ice

i.e., for every precipitation event, a new snow layer is created. For sea ice, the model has a growth rate-dependent salinity profile. The sea ice salinity is a function of growth rate and water salinity [27]. The water underneath the sea ice is kept at constant salinity (32 ppt) and the freezing point of sea water. Snow layer depth is a function of snow load, density, and temperature using Brun *et al.* [5].

B. Sea Ice Emission Model

The output from the thermodynamic model at 6-h time-steps is a snow and sea ice profile including for each layer: average temperature, density, correlation length, salinity, and snow and ice type. The correlation length is a measure of scatter size and distribution [43]. These are all input to the snow and ice emission model which is here a sea ice version of the microwave emission model for layered snow-packs (MEMLS) [42], [26], and hereafter called as the sea ice emission model.

The scattering in FYI is assumed to originate from small brine pockets and the scattering in MYI from small air-bubbles in a matrix of saline ice following recommendations by Shokr [32]. The scattering parameters in the sea ice do not vary in time, and newly formed layers inherit the scatter size from the layer above. Therefore, we assume the correlation length, which is a measure of the microstructure of brine pockets in FYI, to be 0.20 mm throughout the profile and the correlation length of newly formed layers; and air bubble sizes and distribution in MYI to be 0.25 mm. The FYI profile is initiated with a thin 0.01-m saline ice layer with an open 0.005-m layer below. "Open" means that the layer is still forming. The open layer will be closed when it has grown to 0.02-m thickness like all other new layers after that. "Closing" means that the salinity, density, and the correlation length are constrained to given values at the closing of the layer, and a new layer will start forming beneath. Only the temperature of the ice layer is allowed to vary after closing. The density of FYI is set to 920 kg/m^3 and the salinity is a function of the growth rate until the closing. Details are given in Tonboe *et al.* [36]. The initial FYI profile is shown in Table I. The salinity of the top layer of 22 ppt was measured in a sea ice freeze-up experiment in Inglefield Bredning, North Greenland in 2011.

The MYI profile is initiated with a relatively low salinity (0.5–2.5 ppt), and ice thickness of 2.45 m which is isothermal at 270 K in September. The MYI floe at the beginning of the simulation has a 0.05-m nonsaline old snow layer on top of the ice (see Table II). Initially the floe is subdivided into 49 layers, each 0.05-m thick for resolving the temperature profile. New layers are added as MYI grows, and the salinity of those layers is a function of growth rate (similarly to FYI).

The sea ice emission model computes the emissivity and the emitting-layer temperature which are used together with the CLW and WV as input to the atmospheric RTM described in the next section. The output is the TOA T_Bs which are used as input to the c_{ice} algorithms. In addition to the T_B and c_{ice}, the dataset consists of the physical parameters describing the system, including surface emissivity, emitting-layer temperature, snow depth, ice thickness, snow, and sea ice temperature profile. All T_B simulations are at an incidence angle of 55° to comply with most satellite sensor's viewing geometry.

C. Atmosphere and Ocean Emission Model

An RTM model by Wentz and Meissner [41], denoted here as the WM2000 model, is used for simulating the atmospheric emission and absorption for the advanced microwave scanning radiometer (AMSR) selection of channels [41] using Ta, Ws, WV, and CLW over OW. Over sea ice, WV, and CLW are also used, and the surface emissivity e and emitting-layer temperature T_{eff} which are inputs to the WM2000 model are computed in the sea ice emission model. The one-dimensional model setup captures significant emission processes in sea ice even though it does not capture the spatial variability of the sea ice cover caused, for example, by ice convergence resulting in deformation and ridging. Also, it does not include wind redistribution of snow affecting snow depth, density, and grain size, except that the initial density of new snow layers is a function of temperature and Ws [16].

Over OW, the NWP data (Ts, Ws, CLW, and WV) is used directly in the WM2000 model, except that the Ta, which is also used for the surface temperature (Ts), is constrained to a lower temperature of 271.35 K, i.e., all temperatures over OW below the freezing point of seawater are set to 271.35 K [41].

The sequential flow of data is illustrated in the flowchart in Fig. 1 and the input/output of the models is summarized in Table III.

D. Sea Ice Concentration Algorithm Families

Even though there are more than 20 different operational c_{ice} algorithms [11] [15], there are a limited number of algorithms having almost similar sensitivity to the kind of geophysical noise considered in this study. A thorough evaluation of different c_{ice} algorithms is documented in Ivanova *et al.* [15]. Among the algorithm families described in Ivanova *et al.* [15], there are: a) the spectral 18.7 and 36.5 GHz gradient (e.g., Bootstrap-F), b) the polarization difference at either 18.7 or 36.5 GHz (e.g., NASA Team and Bootstrap-P), c) the high frequency at near 90 GHz (e.g., N90LIN), d) the single channel (e.g., 6.9 GHz

TABLE III
INPUT AND OUTPUT OF DATA TO THE MODELS

Model or algorithm	Input	Output
Multilayer snow and sea ice thermodynamical model [39], and [36].	2 m air temperature (Ta) [K], Sea level pressure (P) [hPa], Wind speed 10 m (Ws) [m/s], Incoming short wave radiation (Sw) [W/m^2], Incoming long wave radiation (Lw) [W/m^2], Relative humidity (rh) [1/100], Mass of precipitation (Mr) [kg/m^2]	Profiles: Temperature [K], Density [kg/m^3], Layer thickness [m], Correlation length [mm], Salinity [ppt], Type (new snow, old snow, FYI, MYI)
Sea ice emission model; sea ice version of the Microwave Emission Model for Layered Snowpacks (MEMLS) [42] described in Mätzler et al. [26].	Profiles: Temperature [K], Density [kg/m^3], Layer thickness [m], Correlation length [mm], Salinity [ppt], Type (new snow, old snow, FYI, MYI)	Ice brightness temperature (TB) [K], Ice emissivity (e), Ice emitting layer temperature (T_{eff}) [K]
Atmosphere/ ocean radiative transfer model for simulating the atmospheric emission and absorption at the AMSR channels [41]. Adapted to work over sea ice as well as open water [1].	Over ice: 2 m air temperature (Ta) [K], Total column water vapor in the atmosphere (WV) [kg/m^2], Total column cloud liquid water in the atmosphere (CLW) [kg/m^2], Sea ice emissivity (e), Sea ice emitting layer temperature (T_{eff}) [K], (Sea ice concentration) Over water: Wind speed 10m (Ws) [m/s], Sea surface temperature (SST) [K], 2 m air temperature (Ta) [K], Total column water vapor in the atmosphere (WV) [kg/m^2], Total column cloud liquid water in the atmosphere (CLW) [kg/m^2], (Sea ice concentration)	Top of the atmosphere brightness temperature (TOA T_B) [K]
Eight c_{ice} algorithms	Top of the atmosphere brightness temperature (TOA T_B) [K]	Sea ice concentration (c_{ice}) [1/100]

TABLE IV
CATEGORIZATION OF THE EIGHT SELECTED c_{ICE} ALGORITHMS. THE POLARIZATION ALGORITHMS ARE USING THE POLARIZATION DIFFERENCE OR RATIO. THE GRADIENT ALGORITHMS ARE USING THE SPECTRAL GRADIENT, E.G., AT $T_{B18.7V}$ AND $T_{B36.5V}$. HERE THE LOW FREQUENCY IS 6.9 GHZ AND THE HIGH FREQUENCY IS NEAR 90 GHZ. ESMR WAS SINGLE-CHANNEL (19.35 GHZ H-POL) RADIOMETER ON THE NIMBUS 5 SATELLITE

Algorithm name and reference	Channels:
NASA-Team [10] [11]	18.7 GHz polarization (18.7V, 18.7H, 36.5V)
Bristol [33]	18.7 and 36.5 GHz gradient and polarization (18V, 36V, 36H)
Bootstrap-F [13] [8] [9]	18.7 and 36.5 GHz gradient (18.7V, 36.5V)
Bootstrap-P [13] [8] [9]	36.5 GHz polarization (36.5V, 36.5H)
TUD [29]	18.7V, 36.5V gradient and near 90 GHz polarization (18.7V, 36.5V, 89.0V, 89.0H)
N90LIN [15]	Near 90 GHz polarization (89.0V, 89.0H)
One6H [15]	Low frequency single channel (6.9H)
ESMR [15]	ESMR single channel (18.7H)

H-polarization (One6H)), and e) the hybrids combining gradient and polarization [e.g., Bristol and Technical University of Denmark (TUD)] families. The single-channel algorithms are not real candidates for producing a complete CDR. However, the One6H is included in this study because of its low sensitivity to the atmosphere [15]. Radiometers measuring near-6 GHz were on scanning multichannel microwave radiometer (SMMR) 1978–1987 and on AMSR 2001–2011 and now on AMSR2 2012 onwards. There are also plans to continue the 6-GHz measurements on AMSR-3, and at significantly higher resolution on the Copernicus imaging microwave radiometer [21]. Additionally, the electrically scanning microwave radiometer (ESMR) algorithm, a one-channel algorithm, is included because the ESMR on the NIMBUS 5 satellite covered a time period before modern multifrequency radiometers, from Dec. 1972 to May 1977, and it measured only T_{B19H}. Here the ESMR algorithm is implemented with T_Bs at 18.7 GHz and at a constant incidence angle of 55°. This is a simplification compared to ESMR, which was an across-track scanner measuring at incidence angles between nadir and 63°. The near-19-GHz channel is included on all multifrequency radiometers from 1978 until today. We have selected eight algorithms representing the different families in Table IV.

The polarization (PR) and spectral gradient ratio (GR) used in some c_{ice} algorithms are defined as a function of T_B channel frequency (f) and two polarizations, p_1 and p_2

$$\mathrm{PR}(f,p_1,p_2)=\frac{T_{Bp_1}(f)-T_{Bp_2}(f)}{T_{Bp_1}(f)+T_{Bp_2}(f)} \tag{1}$$

$$\mathrm{GR}(f_1,f_2,p_1)=\frac{T_{Bp_1}(f_1)-T_{Bp_1}(f_2)}{T_{Bp_1}(f_1)+T_{Bp_1}(f_2)} \tag{2}$$

where $f_1 > f_2$.

E. Selected Eight Sea Ice Concentration Algorithms

Our focus here is not on the absolute c_{ice}, but on the c_{ice} noise, and the sensitivity of the algorithms to different noise sources. Therefore, we have not used these eight selected algorithms in their original implementation. For example, in our implementation, the estimated c_{ice} is free to take values above 100% and below 0%, since we wish to study the sensitivity at

TABLE V
TIE-POINTS (TP) FOR THE THREE SURFACE TYPES USED IN THE ALGORITHMS FOR AMSR-E AND THE NORTHERN HEMISPHERE [15]. FOR EXAMPLE, THE $Tp_{6.9H}$ IS THE TIE-POINT AT 6.9 GHZ H-POLARIZATION GIVEN AS THE TOA T_B IN KELVIN

Type	$Tp_{6.9H}$	$Tp_{18.7V}$	$Tp_{18.7H}$	$Tp_{36.5V}$	$Tp_{36.5H}$	$Tp_{89.0V}$	$Tp_{89.0H}$
Open water	82.1	183.7	108.5	209.8	145.3	243.2	196.9
First-year ice	232.1	252.2	237.5	247.1	235.0	232.0	222.4
Multiyear ice	221.2	226.3	207.8	196.9	184.9	187.6	178.9

these reference points and c_{ice} is a near-linear combination of microwave emission from sea ice and water in all algorithms. This implies that the propagation of uncertainty results in approximately normal-distributed noise on c_{ice} and that there are no cut-off thresholds applied at 0% and 100%. A discussion of this argument is included in Refs. [15] and [19].

For the same reasons, some algorithms have been excluded from this investigation because the criteria above could not be met. For example, the NASA Team 2 [25], since the true sensitivity to noise cannot be mapped near the tie-points, and the Artist Sea Ice (ASI) algorithm [17] [34] since it is not linear near the tie-points. Each of the eight algorithms is described in Appendix A.

The eight algorithms in Appendix A take the simulated TOA T_Bs as input and produce c_{ice} as summarized in Table III. For all algorithms, we use a set of consistent AMSR-E tie-points from Ivanova *et al.* [15]; see Table V. The tie-points were derived from the ESA Climate Change Initiative Round Robin Data Package [28].

III. SIMULATION RESULTS

The presentation of the results is divided into seven subsections. In Sections III-A and III-B, we present the FYI and MYI sea ice simulations, respectively. In Section III-C, we compare the simulated T_Bs to observed tie-points in sea ice concentration space; in Section III-D, we describe the atmospheric and surface contribution to the c_{ice} noise; in Section III-E, we investigate the c_{ice} sensitivity to noise over sea ice, and in Section III-F, we describe the c_{ice} sensitivity to noise over OW.

A. FYI in the Ross Sea

Fig. 2 shows the simulated ice growth and snow accumulation as a function of time during Antarctic winter, where T_a is always below 273 K. The ice grows from the initial 0.015 to 1.53 m at the end of the simulation. The snow depth (Hs) is 0.45 m at the end with several major precipitation events during the modeled time frame. The output from the thermodynamic model is input to the sea ice emission model which computes T_Bs (see Fig. 3). Thin ice is present at the beginning of the simulation resulting in lower T_Bs, especially at the low frequencies.

B. MYI in the Lincoln Sea

Fig. 4 shows the simulated ice growth and snow accumulation in the Lincoln Sea as a function of time during the Arctic winter where T_a is below 273.15 K. The MYI grows from the initial isothermal 2.45 to 3.11 m at the end of the simulation. The snow depth increases from the initial 0.05 to 0.37 m with several major precipitation events. The depth of the snow/sea ice interface is decreasing during the simulation because the snow is accumulating faster than the ice grows. The majority of the precipitation events occurred during the initial part of the simulation, and then only two events during mid-winter and some during spring.

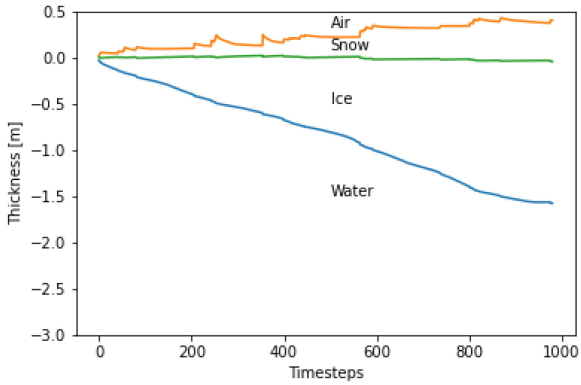

Fig. 2. Simulated ice growth and snow accumulation on the Ross Sea FYI site as a function of time in days since April 1, 2001 (until January 2002). The initial profile is described in Table I.

The simulated T_Bs from the Lincoln Sea MYI profile are shown in Fig. 5. The T_B variability is dominated by the snow and ice temperature but major precipitation events (snow accumulation) are also affecting the variability. Only the simulations between the two vertical lines are included in the c_{ice} analyses. The first 30 days are excluded because the snow layer and temperature profile need to reach equilibrium with the environment before they are comparable to measured T_Bs. The data to the right of the second line are excluded due to air temperatures over 0°C and the thermodynamic model does not have a hydrological module which can handle melt water from the snow layer.

C. Comparison of Simulated Brightness Temperatures to Tie-Points

The tie-points in Table V should fall into the variability range of the simulated T_Bs, and in the ideal case, the tie-points would be in the center of the clusters formed by the simulated T_Bs. We found that different c_{ice} algorithms with the simulated T_B data yielded near 0% c_{ice} for the OW simulations and near 100% c_{ice} for the ice simulations. This indicates that the absolute level of T_B, PR, or polarization difference, and GR in the simulated data are comparable to those in the measured T_B data.

The simulated T_Bs at 18.7 and 36.5 V are shown in Fig. 6, along with the MYI tie-point and ice line for the NH and the FYI tie-point and ice line for the SH [15]. The tie-points are situated

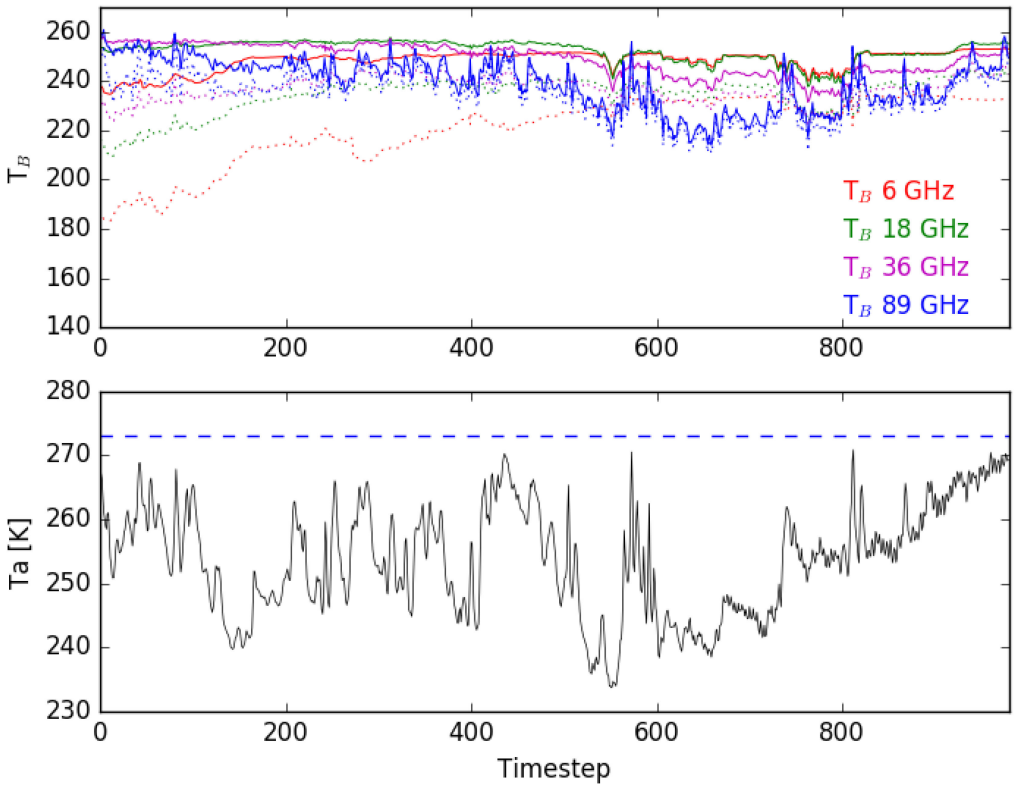

Fig. 3. Upper panel shows the simulated T_Bs at 6.9 (red), 18.7 (green), 36.5 (purple), and 89.0 (blue) GHz at V- (full-line) and H- (dashed-line) polarization in the Ross Sea. The lower panel shows the air temperature, T_a. The horizontal dashed blue line in the lower panel is at 0°C.

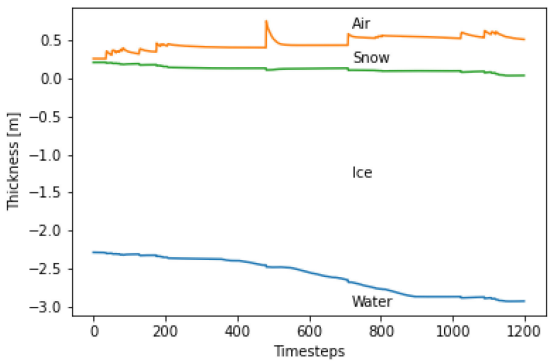

Fig. 4. Simulated ice growth and snow accumulation on the Lincoln Sea MYI site as a function of time in days since September 1. 1999 (until June 2000). The initial profile is described in Table II.

close to the clusters of simulated T_Bs. The Ross Sea simulations are in general higher than the MYI simulations but not quite at the SH ice line, while the Lincoln Sea simulations are clustering around the NH ice line. The OW tie-point from Ivanova *et al.* [15] is in the middle of the elongated OW cluster as expected.

D. Atmospheric and Surface Variability Contribution to Variations in Retrieved c_{ice}

We simulated here in addition to TOA T_Bs also upwelling sea-ice surface emission T_Bs (no atmospheric emission or reflection). The c_{ice} estimates are computed based on these T_Bs to assess the influence of the atmosphere. Tables VI and VII show the mean and standard deviation of the estimated c_{ice} using the TOA and upwelling sea-ice surface emission T_Bs for the eight different c_{ice} algorithms. The direct influence of the atmosphere on the c_{ice} variability at 100% c_{ice} is quantified as the standard deviation of the difference between c_{ice} computed with and without an atmosphere [shortly as STD of the c_{ice} (TOA T_B) and c_{ice} (sea ice self-emission T_B) difference]. It is the smallest, 0.1% and 0.6% in the Lincoln and the Ross Seas, respectively, using the One6H algorithm (see Tables VI and VII). In general, the influence of the atmosphere is increasing with the use of higher frequency channels, i.e., 36.5 GHz (Bootstrap-P) and in particular 89.0 GHz (TUD and N90LIN). The STD of the c_{ice} difference is the largest with the N90LIN c_{ice}; 2.1% and 7.7% in the Lincoln and Ross Seas, respectively. This variability is caused entirely by WV, CLW, and T_a variability through the WM2000 model. This is much less than the noise caused by surface emissivity and effective temperature variability (the "surface noise," given in column "STD c_{ice} excl. atmos."). The atmospheric c_{ice} noise over sea ice is therefore minor except for algorithms only using 89.0-GHz channels. However, the surface noise level is still 1.9 times higher (STD c_{ice} excl. atmos./STD of the c_{ice} diff) than the atmospheric noise level for the N90LIN in the Lincoln Sea (1.8 in the Ross Sea). For all other algorithms, combining 89.0 GHz with lower frequency channels (TUD) or only using lower frequency channels, the surface noise is dominating the total noise level. For example, in the NASA team algorithm using 18.7 and 36.5 GHz channels, the surface noise

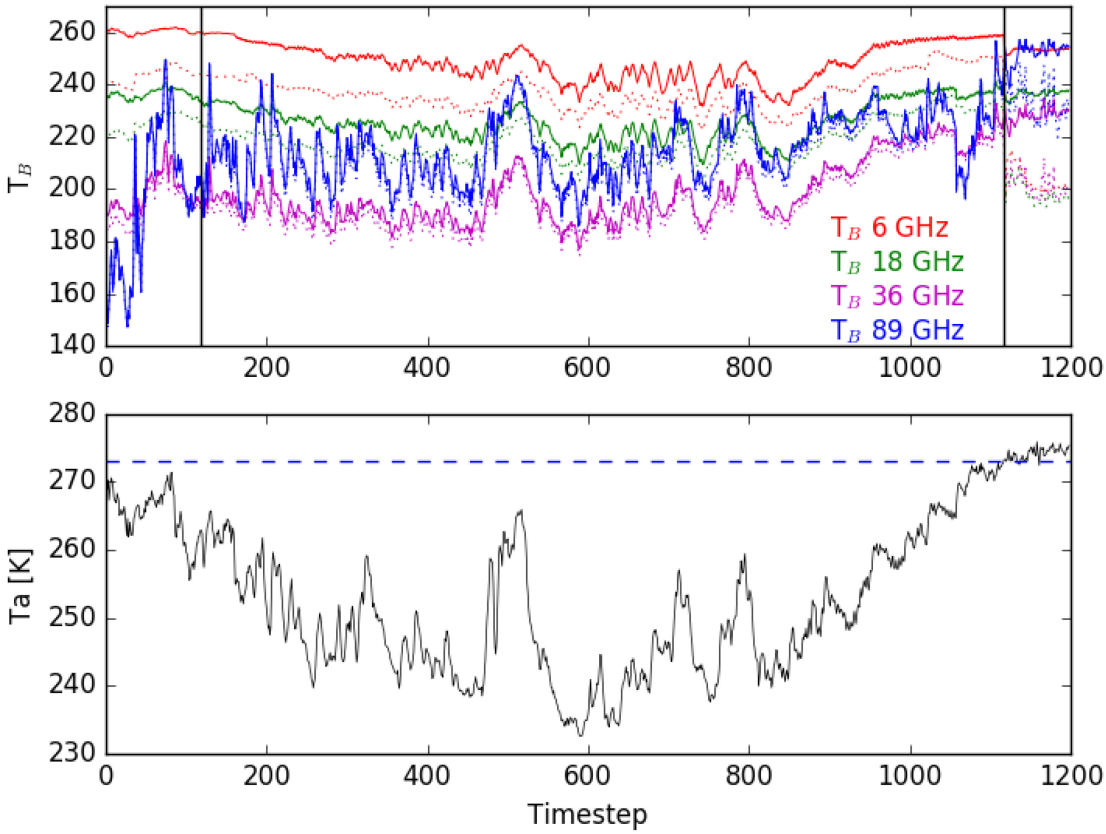

Fig. 5. Upper panel shows the simulated T_Bs at 6.9 (red), 18.7 (green), 36.5 (purple), and 89.0 (blue) GHz at V- (full) and H- (dashed) polarization in the Lincoln Sea. The lower panel shows the air temperature. The horizontal dashed blue line in the lower panel is at 0°C.

TABLE VI
CONTRIBUTIONS TO THE 100 % c_{ICE} VARIABILITY FROM THE ATMOSPHERE AND THE SURFACE FOR THE ROSS SEA FYI PROFILE. COLUMN 1 IS THE MEAN c_{ICE} USING TOP OF THE ATMOSPHERE (TOA) T_BS. COLUMN 2 IS THE STD OF c_{ICE} USING TOA T_BS. COLUMN 3 IS THE MEAN c_{ICE} USING THE UPWELLING SEA ICE SURFACE EMISSION T_BS. COLUMN 4 IS THE STD OF c_{ICE} USING UPWELLING SEA ICE SURFACE EMISSION T_BS. COLUMN 5 IS THE c_{ICE} RATIO BETWEEN USING TOA T_BS AND SEA ICE SURFACE EMISSION T_BS. COLUMN 6 IS THE STD OF THE DIFFERENCE BETWEEN THE c_{ICE} USING TOA AND SEA ICE SURFACE EMISSION T_BS, RESPECTIVELY. ALL VALUES GIVEN IN PERCENT c_{ICE}

Algorithm	Mean c_{ice} incl. atmos. (1)	STD c_{ice} incl. atmos. (2)	Mean c_{ice} excl. atmos. (3)	STD c_{ice} excl. atmos. (4)	Incl. atmos./ excl. atmos. (5)	STD of the c_{ice} diff. (6)
NASA	93.5	11.0	90.9	12.0	1.031	1.3
Bristol	97.6	5.5	95.3	7.1	1.026	1.9
Bootstrap-F	98.4	3.5	98.7	3.7	0.997	0.9
Bootstrap-P	96.4	11.1	89.6	14.3	1.086	3.9
TUD	106.8	4.9	102.8	7.9	1.042	3.9
N90LIN	109.5	8.6	100.2	14.1	1.109	7.7
One6H	95.4	9.8	94.3	10.3	1.013	0.6
ESMR	112.6	6.6	110.5	7.5	1.020	1.3

level is 6.8 and 9.2 times higher than the atmospheric noise level in the Lincoln and the Ross Seas, respectively.

In general, the influence of the atmosphere is an increase in the estimated c_{ice} (compare columns denoted "mean c_{ice} incl. atmos" and "mean c_{ice} excl. atmos.," and values for their ratio "incl. atmos./excl. atmos." greater than one)—except for the gradient type of algorithms (Bootstrap-F, Bristol, TUD); for these, this ratio is less than one (see Table VII) in the Lincoln Sea. In the Ross Sea, only the Bootstrap-F has the incl. atmos./excl. atmos. c_{ice} ratio less than one. The atmosphere in the Lincoln Sea is much drier than that over the Ross Sea. This causes this ratio in the Ross Sea to be higher than in the Lincoln Sea for all algorithms.

Since we are using the same tie-point set for all c_{ice} algorithms, some of them have biases, i.e., the mean c_{ice} is smaller or larger than 100%. These biases could be minimized using the original tie-points for each algorithm or using dynamical tie-points. The biases are so small that the assessment of the atmospheric influence in Tables VI and VII is not affected.

Simulating the microphysical parameters of snow and sea ice such as snow microstructure and the ice salinity profile which affects the microwave emission, and further, the estimated c_{ice} is

TABLE VII
CONTRIBUTIONS TO THE 100 % c_{ICE} VARIABILITY FROM THE ATMOSPHERE AND THE SURFACE FOR THE LINCOLN SEA MYI PROFILE. COLUMN 1 IS THE MEAN c_{ICE} USING TOP OF THE ATMOSPHERE (TOA) T_BS. COLUMN 2 IS THE STD OF c_{ICE} USING TOA T_BS. COLUMN 3 IS THE MEAN c_{ICE} USING THE UPWELLING SEA ICE SURFACE EMISSION T_BS. COLUMN 4 IS THE STD OF c_{ICE} USING UP-WELLING SEA ICE SURFACE EMISSION T_BS. COLUMN 5 IS THE c_{ICE} RATIO BETWEEN USING TOA T_BS AND SEA ICE SURFACE EMISSION T_BS. COLUMN 6 IS THE STD OF THE DIFFERENCE BETWEEN THE c_{ICE} USING TOA AND SEA ICE SURFACE EMISSION T_BS RESPECTIVELY. ALL VALUES GIVEN IN PERCENT c_{ICE}

Algorithm	Mean c_{ice} incl. atmos. (1)	STD c_{ice} incl. atmos. (2)	Mean c_{ice} excl. atmos. (3)	STD c_{ice} excl. atmos. (4)	Incl. atmos./ excl. atmos. (5)	STD of the c_{ice} diff. (6)
NASA	107.7	3.0	107.6	3.4	1.001	0.5
Bristol	113.0	2.4	115.8	2.4	0.976	0.8
Boostrap-F	116.2	4.5	123.0	4.4	0.945	1.0
Bootstarp-P	107.6	2.6	103.6	3.5	1.039	1.2
TUD	117.7	3.1	118.3	3.3	0.995	1.2
N90LIN	112.5	3.2	106.5	4.0	1.057	2.1
One6H	105.0	3.7	104.5	3.7	1.005	0.1
ESMR	107.8	5.4	106.3	5.3	1.015	0.4

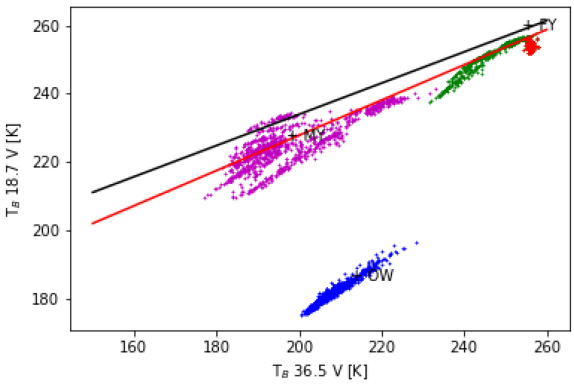

Fig. 6. Simulated TOA T_B 18V vs. the T_B 36.5V for the sea ice in the Lincoln Sea (purple), the Ross Sea (green/red), and open water in the Bellingshausen Sea (blue). For the Ross Sea simulation, all points where the ice thickness is less than 0.3 m are red and points where the ice thickness is larger than 0.3 m are green. The two ice lines for the NH (red) and the SH (black) and the tie-points marked with MYI (NH), FYI (SH), and OW (SH) (from Ivanova *et al.* [15]) are shown for comparison.

a future target for NWP and sea ice models at present [18]. These parameters are typically difficult to measure in the field. On the one hand, the complexity of the atmosphere–snow–sea ice system makes it also difficult to identify and define the important parameters and they are often correlated. On the other hand, the correlation might offer the avenue to reduce the number of parameters that need to be specifically included in such studies.

E. Near 100% Sea Ice Concentration Sensitivity

Fig. 7 shows the computed c_{ice} from eight different algorithms vs. the snow ice interface temperature (T_{si}) for the Ross Sea FYI profile. The focus is here on the co-variation of c_{ice} with T_{si}, not the absolute c_{ice} level (the absolute level can be tuned by adjusting the tie-points to the actual signatures of sea ice and OW). Warm T_{si} ($T_{\text{si}} > 260$ K) are coincident with the part of the simulation where the sea ice is thin, and this results in c_{ice} underestimation for all algorithms also seen in observations, e.g., in [15]. However, warm temperatures ($T_{\text{si}} > 260$ K) could be also caused by other factors than thin ice, like atmospheric warming events. Here it is caused by thin ice only. When the sea ice and snow cover have matured the single channel, gradient and hybrid type of algorithms have a positive correlation with T_{si} while the polarization type of algorithms (NASA and Bootstrap-P) are neutral or the c_{ice} decreases with decreasing T_{si}.

Colder ($T_{\text{si}} < 260K$) T_{si} represents more proper FYI, and much lower correlation between T_{si} and c_{ice} is present; for example, the correlation coefficient between the c_{ice} estimated using Bootstrap-F and the T_{si} is only 0.27. However, other parameters, such as snow and ice thickness, affect the Bootstrap-F c_{ice} at the same time. When removing the linear variability from these parameters using a partial correlation scheme (using the Interactive Data Language $p\_correlate$ function), the Bootstrap-F c_{ice} vs. T_{si} partial correlation coefficient is 0.82, indicating that there is in fact a Bootstrap-F c_{ice} sensitivity to T_{si}. Partial correlations between various snow and sea ice parameters, WV and CLW, and c_{ice} computed with the eight c_{ice} algorithms are shown for the Ross Sea and Lincoln Sea simulations in Figs. 8 and 9, respectively. Partial correlation is the correlation between two variables with the correlation of other variables removed.

Nonlinear relationships make correlation analysis difficult for FYI conditions in the Ross Sea simulation (Fig. 7). However, when looking at the Lincoln Sea profile in Fig. 10, there is a clear almost linear relationship between the one channel algorithms and T_{si}. Slopes of lines fitted to the clusters for One6H is 0.005/K and ESMR 0.007/K. The T_{si} standard deviation is 8.7 K, and within one standard deviation of T_{si} variability, the One6H and the ESMR can have c_{ice} biases of 0.044 and 0.061, respectively. In the following, the one standard deviation bias is given behind the number for sensitivity. There are similar linear relationships between gradient algorithms' c_{ice} (Bootstrap-F 0.007/K and for one STD: 0.061 and Bristol 0.004/K and for one STD: 0.035) and T_{si}. There is a negative correlation between the polarization algorithm c_{ice} and T_{si} (-0.0006/K and for one STD: -0.005): NASA T: $r = -0.76$, and Bootstrap – P: $r = -0.69$. However, the polarization algorithms' c_{ice} variation with respect to T_{si} is very small and there is no systematic relationship. There is no obvious linear relationship or correlation ($r = 0.20$) between the N90LIN c_{ice} and T_{si}.

A similar relationship exists between the Bootstrap-F c_{ice} and the $SnST$ (not shown). Linear relationships between the Bootstrap-F c_{ice} and other parameters are not so obvious.

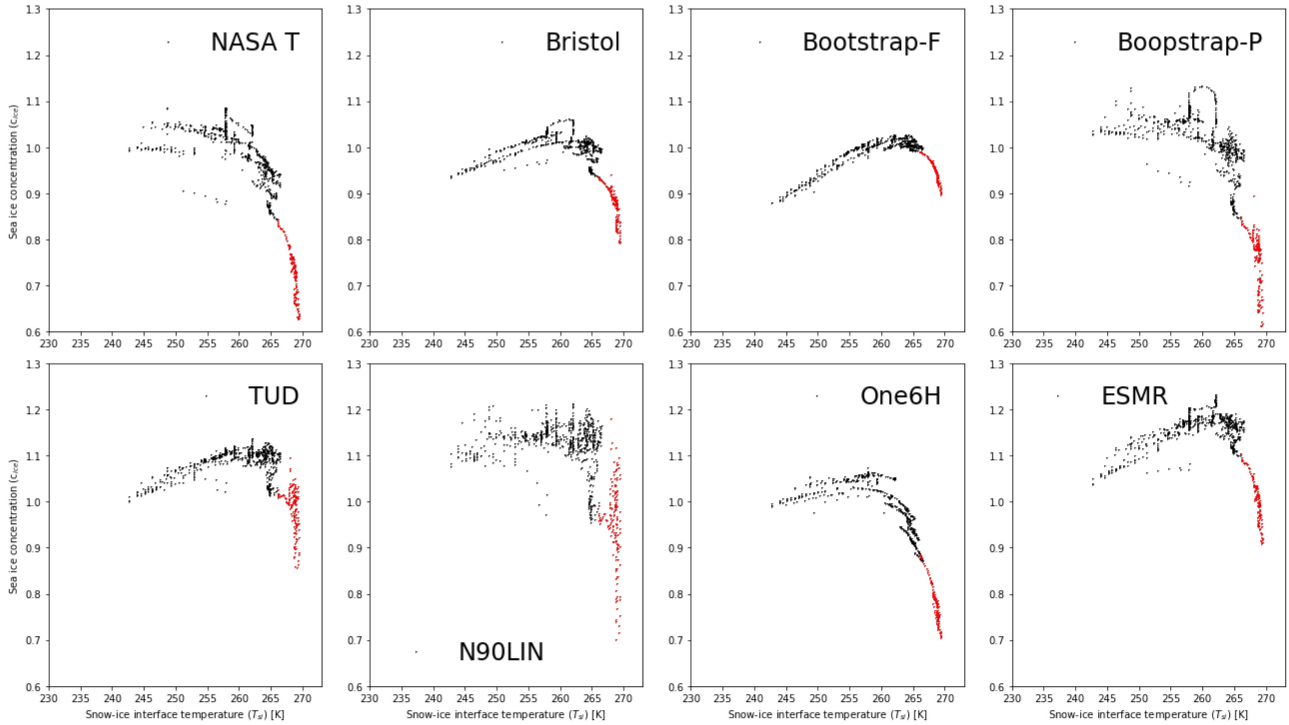

Fig. 7. c_{ice} vs. snow/ice interface temperature (T_{si}) for 100% young ice and FYI in the Ross Sea computed by eight different c_{ice} algorithms. Points where the ice thickness is less than 0.3 m are red.

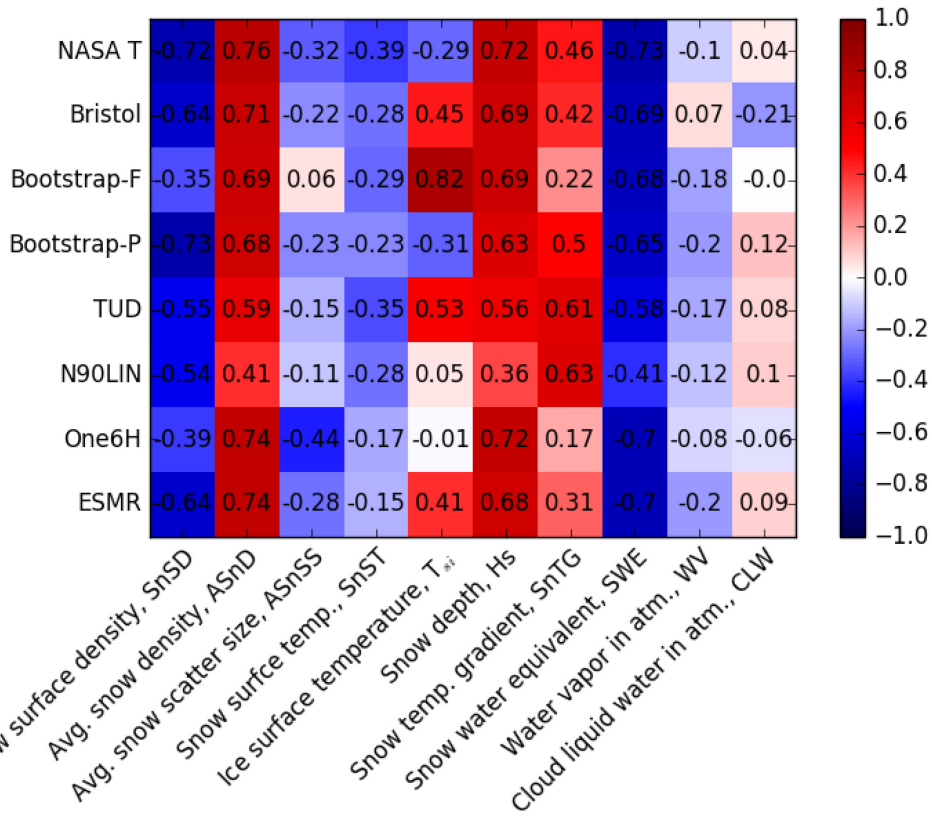

Fig. 8. Partial linear correlations in the Ross Sea between c_{ice} and snow surface density ($SnSD$), average snow density ($ASnD$), average snow scatter size ($ASnSS$), snow surface temperature ($SnST$), snow ice interface temperature (T_{si}), snow depth (Hs), snow temperature gradient ($SnTG$), snow water equivalent (SWE), total water vapor in the atmosphere (WV), and total cloud liquid water in the atmosphere (CLW).

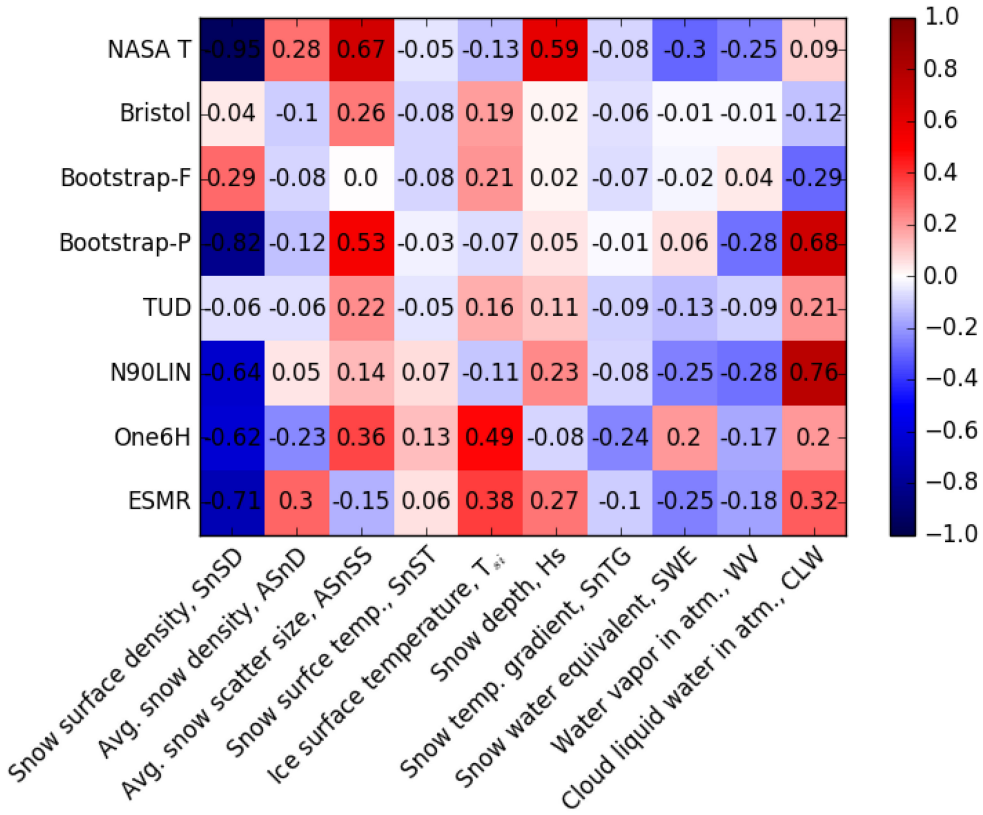

Fig. 9. Partial linear correlations in the Lincoln Sea between c_{ice} and snow surface density ($SnSD$), average snow density ($ASnD$), average snow scatter size ($ASnSS$), snow surface temperature ($SnST$), snow ice interface temperature (T_{si}), snow depth (Hs), snow temperature gradient ($SnTG$), snow water equivalent (SWE), total water vapor in the atmosphere (WV), and total cloud liquid water in the atmosphere (CLW).

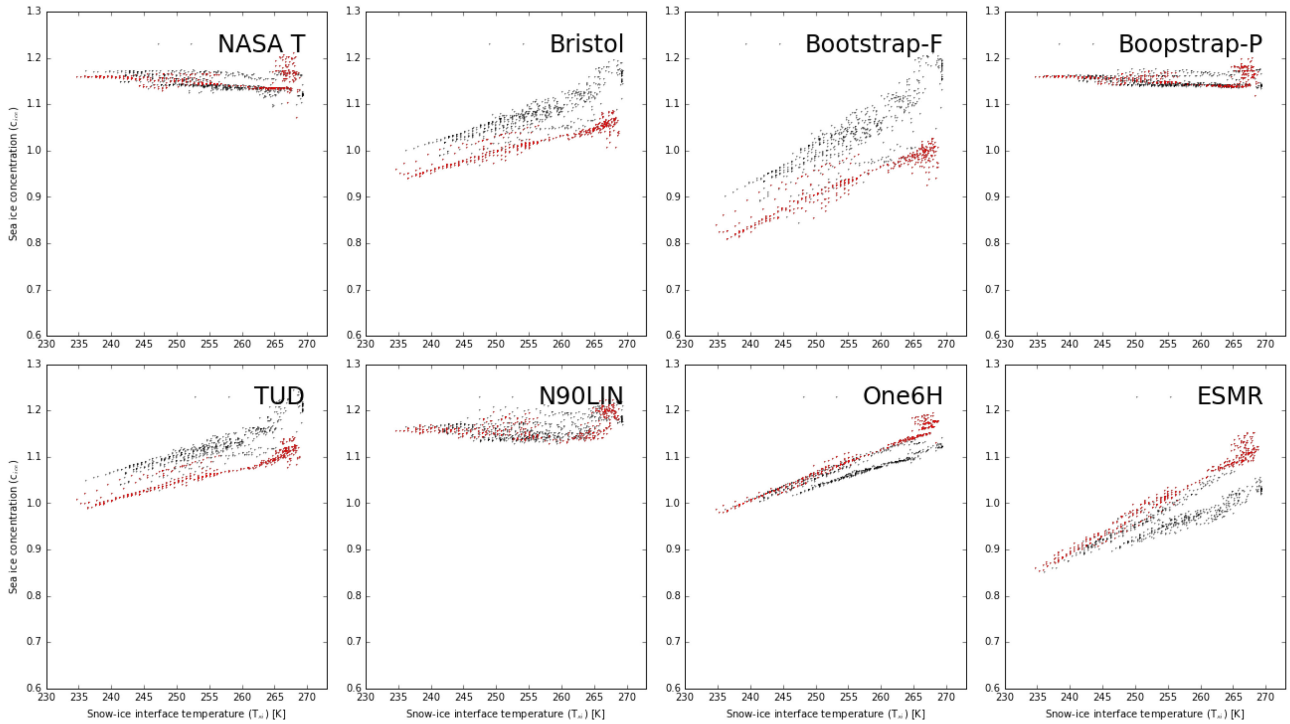

Fig. 10. c_{ice} vs. T_{si} for 100% MYI in the Lincoln Sea calculated by eight different c_{ice} algorithms. Points after a major mid-winter precipitation event (at timestep 588) are red.

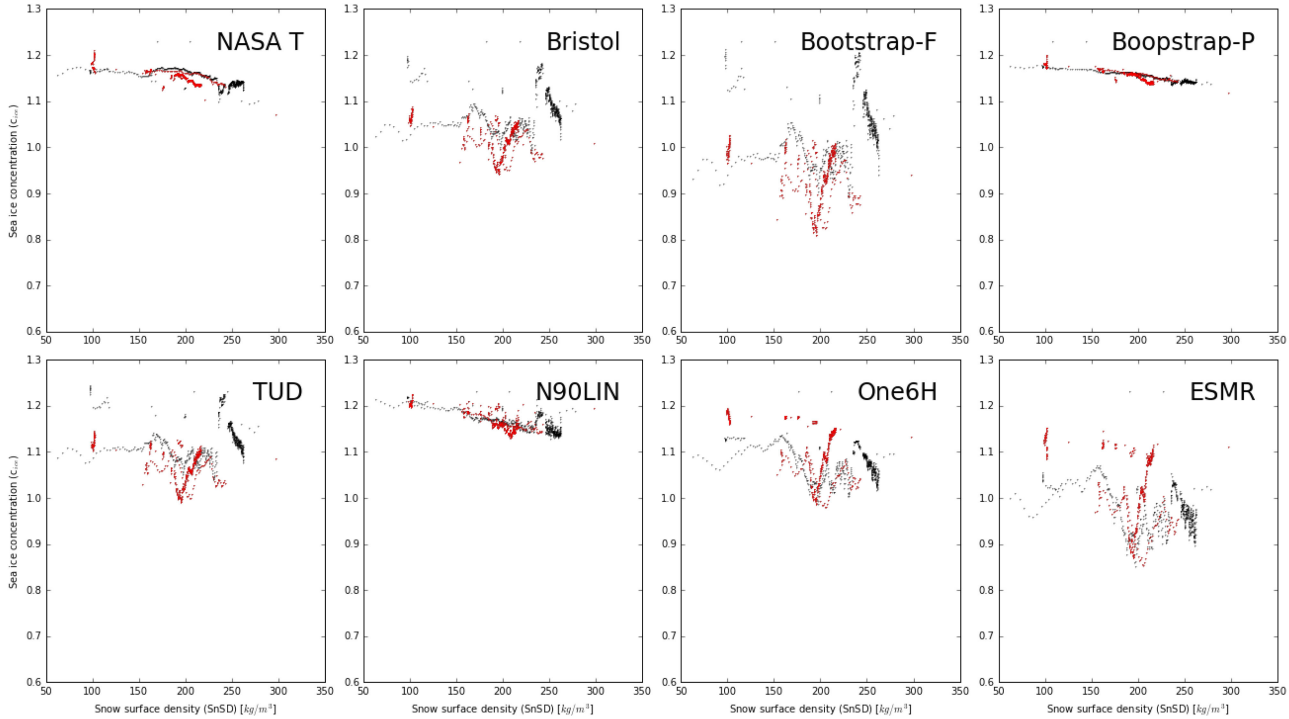

Fig. 11. c_{ice} vs. snow surface density (SnSD) for 100% MYI in the Lincoln Sea for the eight different c_{ice} algorithms. Points after a major mid-winter precipitation event (timestep 588) are red.

The algorithms using polarization difference or ratio directly for computing c_{ice}, i.e., NASA T, Bootstrap- P, and N90LIN, are sensitive to the snow surface density (Fig. 11).

N90LIN c_{ice} is related to snow surface density in line with the simulations in Tonboe and Andersen [35]. For other algorithms that combine the polarization with the spectral gradient or only uses the gradient there is not a strong relationship between the snow surface density ($SnSD$) and the estimated c_{ice}.

Even though the ice conditions in the Lincoln Sea and in the Ross Sea are different, there are similarities in the way the ten physical variables correlate with c_{ice} from the eight different algorithms. If we look at the correlations where the $r^2 > 0.5$ ($|r| >= 0.71$), then the NASA team c_{ice} is correlated with the following snow parameters: snow depth (Hs), snow surface density ($SnSD$), average snow density ($ASnD$), and snow water equivalent (SWE) in the Ross Sea FYI profile. The correlation is positive for Hs and $ASnD$ and negative for $SnSD$ and SWE, i.e., for deeper and more compact snow, the computed c_{ice} increases erroneously. Among these four snow-cover parameters, the sign (negative or positive correlation) is consistent for the NASA team algorithm and both for the Lincoln Sea and the Ross Sea profiles. For all algorithms, c_{ice} is negatively correlated with $SnSD$ but positively correlated with $ASnD$ for the Ross Sea FYI profile (Fig. 8). This consistency is not the case for the Lincoln Sea MYI profile, where the respective partial correlations tend to be much smaller for most of the algorithms (Fig. 9).

The $SnSD$, which is a proxy for snow-pack layering, has a negative partial correlation with the polarization type of algorithms NASA Team and Bootstrap-P. Also, the ESMR c_{ice} is negatively correlated with the $SnSD$. Bootstrap-F is the only algorithm showing a particularly high partial correlation (+0.82) with T_{si} in the Ross Sea FYI profile. This is accompanied with the lowest correlation (-0.35) with $SnSD$ in contrast to Bootstrap-P, which actually shows the highest partial correlation (-0.73) here.

The effect of increasing WV and CLW over sea ice is clear: It gives higher c_{ice}. This is, however, not clear from the partial correlations because other parameters dominate the variability, i.e., the atmospheric c_{ice} noise plays a minor role over sea ice. The effect of the surface is ambiguous. None of the surface parameters are clearly characterizing the emission processes alone and there is a really complicated inter-correlation and relationships are different for different ice types and snow depths.

F. Open Water (0% c_{ice}) results

In the WM2000 model, the T_Bs are a function of the Ta, sea surface temperature, CLW, WV, and Ws. The T_B sensitivity to these physical parameters is propagated very differently into the eight c_{ice} algorithms. Fig. 12 shows c_{ice} sensitivity to WV. The estimated c_{ice} from all algorithms except Bootstrap-F and TUD increase as a function of increasing WV. Slopes of lines fitted to the clusters in Fig. 12 are an approximate measure of the c_{ice} WV sensitivity and these and the sensitivity multiplied by one WV standard deviation are given in brackets behind each algorithm in the following. The One6H (0.008/kg m $^{-2}$ and for one STD: 0.025) may have a small apparent sensitivity to WV due to the natural correlation between WV and surface temperature, i.e., it is sensitive to surface temperature and not WV. The Bootstrap-P

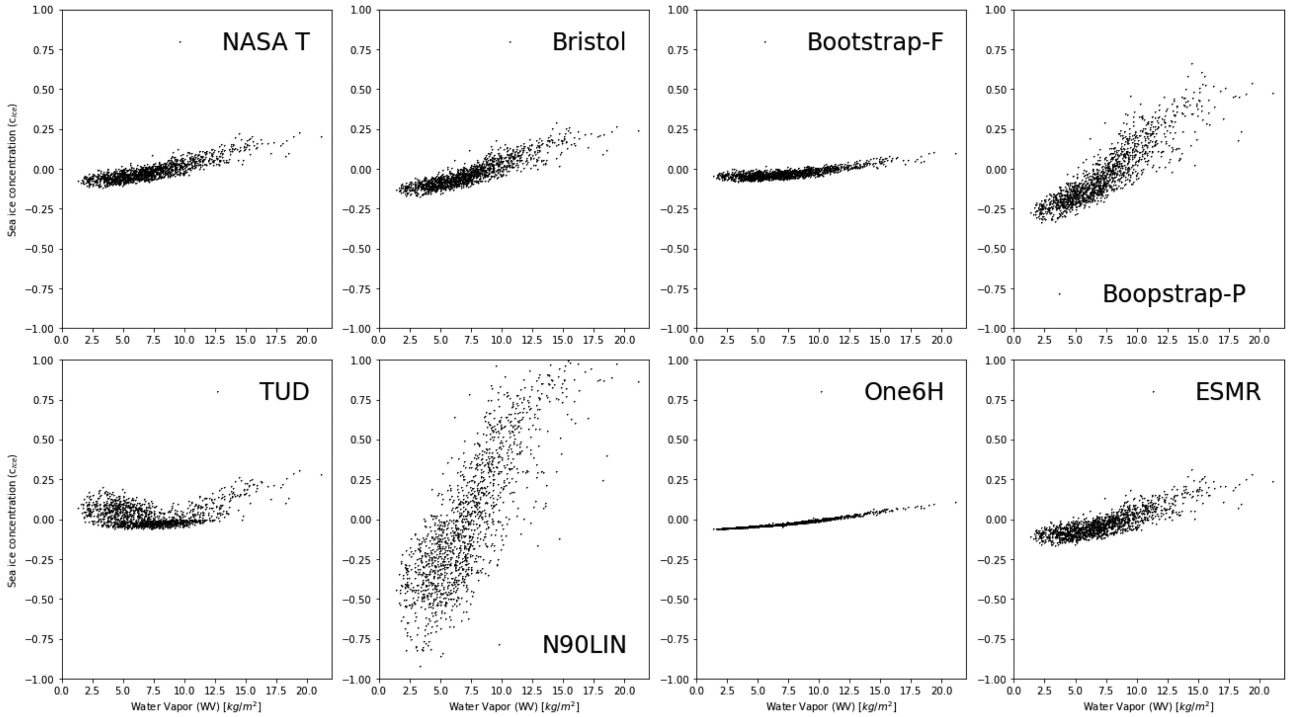

Fig. 12. Sea ice concentration, c_{ice}, from simulated open water T_Bs vs. total water vapor in the atmosphere.

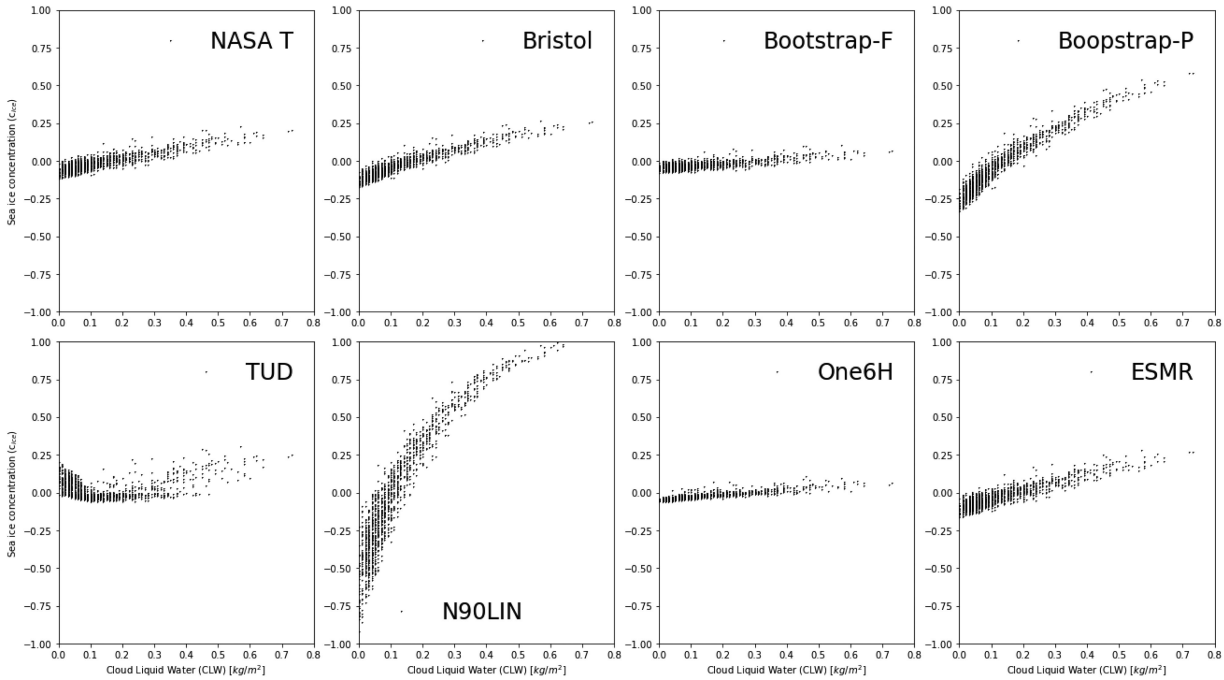

Fig. 13. Simulated open water c_{ice} vs. CLW content in the atmosphere. The stripes in the clusters are caused by the CLW data at 0.01 kg/m^2 quantization.

(0.051/kg m^{-2} and for one STD: 0.158) and in particular the N90LIN (0.105/kg m^{-2} 0.326) algorithms are very sensitive to WV. Our results over OW (0% c_{ice}) conditions using simulated T_B s are well in line with the conclusions by Ivanova *et al.* [15] who used actual T_B measurements [28].

The CLW is one of the parameters which are very difficult to quantify adequately in NWP and re-analysis models at the spatial and temporal scale of satellite radiometer measurements. It is therefore very important to find a c_{ice} algorithm, which is not too sensitive to CLW [4]. Among the eight c_{ice} algorithms,

both the Bootstrap-F (0.16/kg m^{-2} and for one STD: 0.021) and One6H (0.18/kg m^{-2} and for one STD: 0.023) and also the NASA Team (0.40/kg m^{-2} 0.052) have low sensitivity to CLW (Fig. 13). On the contrary, the N90LIN (2.92/kg m^{-2} and for one STD: 0.38) is very sensitive to CLW.

All algorithms except Bootstrap-P and N90LIN have low to moderate sensitivity to both WV and CLW over OW. Bootstrap-P c_{ice} is a function of both VW (0.05/kg m^{-2}) and CLW (1.36/kg m^{-2}). N90LIN c_{ice} is very sensitive to WV (0.11/kg m^{-2}) and CLW (2.93/kg m^{-2}).

IV. Conclusion

Main requirements to c_{ice} algorithms over sea ice for making CDRs are as follows.

1) Low sensitivity to surface noise (sea ice surface emissivity and effective temperature variability);
2) low sensitivity to weather [WV and CLW in the atmosphere and OW surface wind (wind not investigated in this study)];
3) adjustment to climatological changes in noise terms (dynamically derived tie-points), and therefore;
4) low sensitivity to the selection of tie-points (the algorithm is linear both at intermediate concentrations and near the tie-points); and
5) data from the SMMR period 1978-1987 (no near-90 GHz channels) and SSM/I F8 1987-1991 (no 6 GHz channels and partly dysfunctional near-90 GHz channels) can be used thus extending the CDR; and finally,
6) there may be requirements to spatial and radiometric resolution.

In this study, we investigated 1) and 2) that are dealing with the c_{ice} algorithm stability. The stability depends on the overall algorithm c_{ice} sensitivity to all noise sources, and in particular to the noise sources that are not possible to quantify and correct, and result in systematic uncertainties. NWP fields of WV, wind speed over OW, and surface temperature have been used successfully together with an RTM to reduce noise in c_{ice} estimates [1], [37], [22]. However, in these studies, there was no explicit correction for any sea ice variables or for CLW. Such a correction would require a sea ice emissivity model and accurate estimates of snow cover, ice thickness and internal/microwave emitting-layer temperature, and accurate CLW representation in NWP models. Long time-series of these variables are required for reducing the remaining noise in c_{ice} CDRs and are not yet available at the temporal and spatial resolution of the radiometers which we use to derive c_{ice}. Among these variables, T_{si} may be the most accessible in future from either NWP or satellite measurements [12], [20], [31].

The simulated T_Bs from the three cases are comparable to typical signatures (tie-points and ice line) of FYI, MYI, and OW in Section III-C. These T_Bs are input to eight different c_{ice} algorithms, each representing different algorithm families, i.e., different methodologies for deriving c_{ice} from satellite T_Bs. The selection of the T_B channels as input to the c_{ice} algorithms is most important when avoiding noise in the c_{ice} estimates.

The c_{ice} sensitivity is separated into surface and atmospheric contributions over sea ice, and physical dependence between different snow and sea ice parameters was analyzed in this study.

A. Simulated Brightness Temperatures, T_Bs

The absolute level of simulated FYI T_Bs in the Ross Sea is slightly lower than measurements/tie-points throughout the cold period (Fig. 6) while the simulated MYI T_Bs in the Lincoln Sea are comparable to the MY tie-point/ice line. There are several ways that our sea ice emission model could yield higher T_Bs: a) an increase of the emitting layer temperature; b) an decrease of the total reflectivity, for example, less layering in the snow pack, and c) an decrease of volume scattering by decreasing the scattering layer depth by increasing temperature and/or salinity or decreasing the scatter size in the snow or ice. a) and b) are constrained by the thermodynamic model, and the mechanisms described in c) are likely candidates for increasing the simulated Ross Sea T_Bs to the observed tie-point level. The air-bubble correlation length in the multiyear ice has here been set to 1.25 mm in the upper 5-cm ice layer, implying a high level of scattering in the ice, which is approximately resulting in T_Bs at the observed level at frequencies affected by volume scattering. To our knowledge, no *in situ* measurements of the sea ice correlation length exist and the sea ice microstructure can be quite variable [23].

In Fig. 6, neither the cluster of FYI nor MYI points are distributed exactly along a straight line (the ice line). The nonlinearities will result in systematic c_{ice} biases using, for example, the Bootstrap-F algorithm. Low T_Bs are in general caused by low physical temperatures, high reflectivity and by elevated scattering in the snow and ice. This affects the 18.7- and 36.5-GHz emission differently because of different penetration depth across the physical temperature profile and the different scattering magnitudes at the two frequencies. This is an important result since many c_{ice} algorithms (e.g., Bootstrap-F and Bristol) are based on the hypothesis of a straight ice line capturing the variability of surface emissivity with sea-ice type. Our simulation results suggest that higher accuracies can be reached by revisiting the concept of the ice line in c_{ice} algorithms, as was recently explored by Lavergne *et al.* [22]. Large footprints of satellite radiometers yield T_B signatures which are very rarely originating from only one ice type [39]. Cracks and leads in MYI are filled with new-ice during winter and FYI is mixed with MYI (e.g., in the Fram Strait and Greenland Sea). These mixtures would actually result in points being closer to the ice line in Fig. 6.

Still in Fig. 6, the new/young ice points (green in Fig. 6) are within a cluster perpendicular to the ice line. This actually results in erroneously low c_{ice} over new/young ice [15]. Simulations (not shown) indicate that the reflectivity of new ice and the absence of a snow cover is a major factor for the T_B signatures and results in low c_{ice} with a number of algorithms.

B. Atmosphere Contribution

We found that the atmosphere plays a minor role over sea ice, except for the algorithms exclusively using the 89-GHz channels

and that the influence of the atmosphere is an increase in the computed c_{ice} except for the Bootstrap-F algorithm which has a mean atm./no atm. c_{ice} ratio less than one (see Tables VI and VII) both for the Ross Sea and the Lincoln Sea profiles, even though the surface T_Bs over FYI are larger than those over MYI, and therefore, the relative importance of the atmospheric emission is larger over MYI. This is because the atmosphere in the Lincoln Sea is much colder and drier than the atmosphere over the Ross Sea and this causes the ratio of c_{ice} with and without atmosphere in the Ross Sea to be higher than in the Lincoln Sea (even for the Bootstrap-F which is 0.945 in the Lincoln Sea and 0.997 in the Ross Sea).

In OW conditions, our simulation results confirm those of, e.g., Ivanova *et al.* [15] that different algorithms and channel combinations give very different sensitivity to atmosphere and ocean surface emissivity contributions. Wind speed, WV and SSTs are reliable enough from NWP reanalysis to allow explicit correction with an RTM [1], [37], [22]. Other variables like CLW are difficult to correct explicitly for, and it is better to select algorithms that are less sensitive to this effect.

C. Sea Ice Concentration Algorithm Stability and Sea Ice Climate Data Records

The spectral gradient type of algorithms, e.g., Bootstrap-F, are sensitive to the emitting-layer temperature and T_{si} (Fig. 8). The polarization type of algorithms, e.g., Bootstrap-P, are sensitive to snow-pack layering, and the near-90-GHz algorithms are sensitive to weather (WV and CLW), in addition to the snow surface variables, in particular $SnSD$. These sensitivities have been confirmed and investigated in detail in this study. While snow layering is very difficult to quantify even using contemporary satellite sensors, $SnST$ and T_{si} might be within reach also on longer timescales [20], [31]. Here, the $SnSD$ has been used as a proxy for the snow-pack layering and it is certainly related to the air–snow interface reflection. However, internal reflections and scattering within the snow-pack and the snow-ice interface reflection are not quantified by $SnSD$ only.

Due to their low sensitivity to noise the Bristol, Bootstrap-F and TUD algorithm families are good candidates for a CDR c_{ice} algorithm. However, one disadvantage of the TUD algorithm is that it relies on the near-90-GHz channels, which are available without interruption only from 1991 and onwards. The single-channel algorithms (One6H and ESMR) are in spite of their simplicity performing reasonably well in terms of sensitivity to T_{si} and STD of c_{ice}, especially the One6H. However, large gaps in the near-6-GHz data record since 1978 prevent using this algorithm continuously over time. It is also worth noticing that c_{ice} from different algorithms have different sensitivity to noise, and combining different algorithms for a CDR may result in diverse artificial trends. We need to mitigate the noise, if possible, and we would also like to construct relatively simple sea ice emission models where the T_Bs are a function of a relatively limited set of variables which are suitable for model inversion and statistical retrieval.

Several of the parameters needed for reducing the noise level in the c_{ice} estimates over sea ice using T_Bs are available in sea ice numerical models. Assimilation of T_Bs does reduce noise in model c_{ice} estimates [30]. These results are promising and the ESA sea ice CCI project has been working toward the development of observation operators (RTMs) for T_B assimilation in numerical ocean and sea ice models and for optimal estimation schemes. These models may help reduce the sensitivities of c_{ice} algorithms to various noise sources [6] [7].

D. Conclusions

The main conclusions are summarized.

- The simulated clusters of MYI and FYI T_Bs are distributed along the ice line and the simulated OW T_Bs are centered around the OW tie-point, which means that the model system is capable of simulating realistic ice and OW T_Bs.
- The c_{ice} noise over ice is dominated by surface processes and not variability in the atmospheric WV, CLW and T_a even for the high-frequency algorithms (e.g., N90LIN), where the atmospheric influence only amounts to about 1/3 of the total noise.
- Over ice, the c_{ice} algorithms using the polarisation difference or polarization ratio (N90LIN, NASA Team, Bootstrap-P) are sensitive to the snow surface density, and the single-channel and spectral-gradient algorithms (One6H, ESMR, Bristol, Bootstrap-F) are sensitive to variations in the snow ice interface temperature, T_{si}.
- Over OW, Bootstrap-F and One6H have low sensitivity to both WV and CLW. NASA Team, Bristol, TUD, and ESMR have moderate sensitivity while Bootstrap-P has high sensitivity and N90LIN very high sensitivity to WV and CLW.
- The Bristol, Bootstrap-F and TUD algorithm families are candidates for a CDR c_{ice} algorithm, or part of a hybrid algorithm, due their low sensitivity to noise over ice and OW. However, TUD is limited due to the near-90-GHz channels being available only after 1991.
- The emitting-layer temperature or the T_{si} are good candidates for new variables to be included in T_B noise reduction schemes before computing c_{ice} and could potentially improve the estimates from Bristol and Bootstrap-F algorithms and improve CDR stability.

APPENDIX A

Bootstrap-F is the one part of the original Bootstrap algorithm, which is typically used over OW [13], [8], [9]. The slope of the ice line in (3) is computed based on the tie-points ($Tp^{\text{ice type}}_{\text{channel}}$) for FYI and MYI and at 18.7 and 36.5 GHz V-polarization.

$$a = \frac{Tp^{\text{FY}}_{36\text{V}} - Tp^{\text{MY}}_{36\text{V}}}{Tp^{\text{FY}}_{18\text{V}} - Tp^{\text{MY}}_{18\text{V}}}. \tag{3}$$

The ice line offset is computed in (4).

$$b = Tp^{\text{MY}}_{36\text{V}} - a \times Tp^{\text{MY}}_{18\text{V}}. \tag{4}$$

Then, we compute the slope q in (5) and off-set w in (6) of the line connecting the ice line and the OW tie-point passing

through the point where we want to compute c_{ice}

$$q = \frac{T_{B37\text{V}} - Tp_{37V}^{\text{OW}}}{T_{B18\text{V}} - Tp_{18\text{V}}^{\text{OW}}} \tag{5}$$

$$w = Tp_{37\text{V}}^{\text{OW}} - q \times Tp_{18\text{V}}^{\text{OW}}. \tag{6}$$

Combining (3)–(6), we have

$$Ti_{18\text{V}37\text{V}} = \frac{b - w}{q - a} \tag{7}$$

where $Ti_{18\text{V}37\text{V}}$ is the intercept between the ice line and the line going through the OW tie-point and the measured T_B. Now $Ti_{18\text{V}37\text{V}}$ can act as the ice tie-point and we can estimate the total c_{ice} with a one-dimensional scaling algorithm

$$c_{\text{ice}} = \frac{T_{B18\text{V}} - Tp_{18\text{V}}^{\text{OW}}}{Ti_{18\text{V}37\text{V}} - Tp_{18\text{V}}^{\text{OW}}}. \tag{8}$$

Bootstrap-P is another part of the original Bootstrap algorithm and it is typically used over high c_{ice} [13]. Bootstrap-P uses the same methodology as Bootstrap-F except that it is using only the 36 GHz V- and H-polarization channels instead of the 18 and 37 V-polarization channels.

The original TUD algorithm uses Bootstrap-F in combination with the scaled near-90-GHz polarization difference over ice [29]

$$c_{89} = 1.35 + \frac{T_{B89\text{V}} - T_{B89\text{H}}}{40} \tag{9}$$

and

$$c_{\text{ice}} = \sqrt{c_{\text{ice}}(Bootstrap - F) \times c_{89}} - 0.03. \tag{10}$$

Since c_{89} in (9) and $c_{\text{ice}}(Bootstrap - F)$ in (8) are in themselves independent estimates of c_{ice}, (10) is reducing random noise in addition to taking advantage of the higher spatial resolution at 89 GHz. If the $c_{\text{ice}}(Bootstrap - F)$ is less than 0, then c_{ice} equals $c_{\text{ice}}(Bootstrap - F)$.

The empirical coefficients in (9) and (10) are determined by regression of the 89-GHz polarization difference vs. Bootstrap-F c_{ice}. The 0.03 in (10) was introduced when switching from SSMI (85 GHz) to AMSR (89 GHz).

The Near90LIN is simply a linear combination of the polarization difference at the near-90-GHz channels [15]

$$c_{\text{ice}} = 1.22673 - 0.02652(T_{B89\text{V}} - T_{B89\text{H}}). \tag{11}$$

The One6H is a one-dimensional scaling of the 6.9-GHz H-polarization T_B [15]. Here the ice tie-point is the average of the MYI and FYI tie-points (Tp_{6H}^{ice})

$$Tp_{6\text{H}}^{\text{ice}} = (Tp_{6\text{H}}^{\text{FYI}} + Tp_{6\text{H}}^{\text{MYI}})/2 \tag{12}$$

and

$$c_{\text{ice}} = \frac{T_{B6\text{H}} - Tp_{6\text{H}}^{\text{OW}}}{Tp_{6\text{H}}^{\text{ice}} - Tp_{6\text{H}}^{\text{OW}}}. \tag{13}$$

The ESMR single-channel $T_{B18\text{H}}$ algorithm is also a one-dimensional scaling algorithm [15]

$$Tp_{18\text{H}}^{\text{ice}} = (Tp_{18\text{H}}^{\text{FY}} + Tp_{18\text{H}}^{\text{MY}})/2 \tag{14}$$

and

$$c_{\text{ice}} = \frac{T_{B18\text{H}} - Tp_{18\text{H}}^{\text{OW}}}{Tp_{18\text{H}}^{\text{ice}} - Tp_{18\text{H}}^{\text{OW}}}. \tag{15}$$

ACKNOWLEDGMENT

The authors would like to thank the two anonymous reviewers for valuable comments that improved the manuscript. The work described in this manuscript is part of the effort in the ESA CCI project to improve sea ice CDRs.

REFERENCES

[1] S. Andersen, R. Tonboe, S. Kern, and H. Schyberg, "Improved retrieval of sea ice total concentration from spaceborne passive microwave observations using Numerical Weather Prediction model fields: An intercomparison of nine algorithms," *Remote Sens. Environ.* vol. 104, pp. 374–392, 2006.

[2] F. J. Wentz and M. Schabel, "Precise climate monitoring using complementary satellite data sets," *Nature* vol. 403, pp. 414–416, 2000.

[3] A. Beitsch, "Uncertainties of a near 90 GHz sea ice concentration retrieval algorithm," Ph.D. Dissertation, Univ., p. 123, 2014. [Online]. Available: https://ediss.sub.uni-hamburg.de/bitstream/ediss/5673/1/Dissertation.pdf

[4] S. Andersen, L. T. Pedersen, G. Heygster, R. Tonboe, and L. Kaleschke, "Intercomparison of passive microwave sea ice concentration retrievals over the high concentration Arctic Sea ice," *J. Geophysical Res.*, vol. 112, 2007, Art. no. C08004.

[5] E. Brun, E. Martin, V. Simon, C. Gendre, and C. Coleou, "An energy and mass model of snow cover suitable for operational avalanche forecasting," *J. Glaciol.*, vol. 35, No 121, pp. 333–342, 1989.

[6] C. Burgard, D. Notz, L. T. Pedersen, and R. T. Tonboe, "The Arctic ocean observation operator for 6.9 GHz (ARC3O) – Part 1: How to obtain sea ice brightness temperatures at 6.9 GHz from climate model output," *Cryosphere*, vol. 14, pp. 2369–2386, 2020.

[7] C. Burgard, D. Notz, L. T. Pedersen, and R. T. Tonboe, "The Arctic ocean observation operator for 6.9 GHz (ARC3O) – Part 2: Development and evaluation," *Cryosphere*, vol. 14, pp. 2387–2407, 2020.

[8] J. C. Comiso, "SSM/I Sea ice concentration using the bootstrap algorithm," *NASA Reference Publicat.*, 1995, vol. 1380, pp. 1–40.

[9] J. C. Comiso, D. J. Cavalieri, C. L. Parkinson, and P. Gloersen, "Passive microwave algorithms for sea ice concentration: A comparison of two techniques," *Remote Sens. Environ.*, vol. 60, pp. 357–384, 1997.

[10] D. J. Cavalieri, P. Gloersen, and W. J. Campbell, "Determination of sea ice parameters with the Nimbus 7 SMMR," *J. Geophysical Res.* vol. 89, no. D4, pp. 5355–5369, 1984.

[11] D. J. Cavalieri, K. M. St Germain, and C. T. Swift, "Reduction of weather effects in the calculation of sea ice concentration with the DMSP SSM/I," *J. Glaciol.*, vol. 41, pp. 455–464, 1995.

[12] J. C. Comiso, D. J. Cavalieri, and T. Markus, "Sea ice concentration, ice temperature, and snow depth using AMSR-E data," *IEEE Trans. Geosci. Remote Sens.*, vol. 41, no. 2, pp. 243–252, Feb. 2003.

[13] J. C. Comiso, "Characteristics of Arctic winter sea ice from satellite multispectral microwave observations," *J. Geophysical Res.*, vol. 91, no. C1, pp. 975–994, 1986.

[14] R. Hollmann *et al.*, "The ESA climate change initiative/article-title," *Bull. Amer. Meteorol. Soc.*, vol. 94, no 10, pp. 1541–1552, 2013.

[15] N. Ivanova *et al.*, "Inter-comparison and evaluation of sea ice algorithms: Towards further identification of challenges and optimal approach using passive microwave observations," *Cryosphere*, vol. 9, pp. 1797–1817, 2015.

[16] R. Jordan, E. Andreas, and A. Makshtas, "Heat budget of snow covered sea ice at North Pole 4," *J. Geophysical Res.* vol. 104, no. C4, pp. 7785–7806, 1999.

[17] L. Kaleschke *et al.*, "SSM/I ice remote sensing for mesoscale ocean-atmosphere interaction analysis," *Can. J. Remote Sens.*, vol. 27, no. 5, pp. 526–537, 2001.

[18] E. J. Kang, B. J. Sohn, R. Tonboe, G. Dybkjær, K. Holmlund, J.-M. Kim, and C. Liu, "Implementation of a 1-D thermodynamical model for simulating the winter-time evolvement of physical properties of snow and ice over the Arctic Ocean," *J. Adv. Modelling Earth Syst.*, vol. 13, 2021, Art. no. e2020MS002448.

[19] S. Kern *et al.*, "Satellite passive microwave sea-ice concentration data set intercomparison: Closed ice and ship-based observations," *Cryosphere*, vol. 13, pp. 3261–3307, 2019.
[20] L. Kilic, R. Tonboe, C. Prigent, and G. Heygster, "Estimating the snow depth, the snow-ice interface temperature, and the effective temperature of Arctic sea ice using advanced microwave scanning Radiometer 2 and ice mass balance Buoy data," *Cryosphere*, vol. 13, pp. 1283–1296, 2019.
[21] L. Kilic *et al.*, "Expected performances of the Copernicus Imaging Microwave Radiometer (CIMR) for an all-weather and high spatial resolution estimation of ocean and sea ice parameters," *J. Geophysical Res.: Oceans*, vol. 123, pp. 7564–7580, 2018.
[22] T. Lavergne *et al.*, "Version 2 of the EUMETSAT OSI SAF and ESA CCI sea-ice concentration climate data records," *Cryosphere*, vol. 13, pp. 49–78, 2019.
[23] R. M. Lieb-Lappen, E. J. Golden, and R. W. Obbard, "Metrics for interpreting the microstructure of sea ice using X-ray micro-computed tomography," *Cold Regions Sci. Technol.*, vol. 138, pp. 24–35, 2017.
[24] J. Lu, G. Heygster, and G. Spreen, "Atmospheric correction of sea ice concentration retrieval for 89 GHz AMSR-E observations," *IEEE J-STARS*, vol. 11, pp. 1442–1457, 2018.
[25] T. Markus and D. Cavalieri, "An enhancement of the NASA Team sea ice algorithm," *IEEE Trans. Geosci. Remote Sens.*, vol. 38, no. 3, pp. 1387–1398, May 2000.
[26] C. Mätzler, P. W. Rosenkranz, A. Battaglia, and J. P. Wigneron, Eds. "Thermal microwave radiation - Applications for remote sensing," *IEE Electromagn. Waves Ser.*, London, U.K., vol. 52, pp. 583, 2006.
[27] M. Nakawo and N. K. Sinha, "Growth rate and salinity profile of first-year sea ice in the high Arctic," *J. Glaciol.*, vol. 27, no. 96, pp. 315–330, 1981.
[28] L. T. Pedersen, *et al.*, "Reference dataset for sea ice concentration," 2018, [Online]. Available: https://figshare.com/articles/dataset/Reference_dataset_for_sea_ice_concentration/6626549.
[29] L. T. Pedersen, "Development of new satellite ice data products," (Chapter 6.2) Nansen Environmental and Remote Sensing Center, Bergen, Norway, NERSC Tech. Rep. 145, 1998.
[30] K. A. Scott, M. Buehner, A. Caya, and T. Carriers, "Direct assimilation of AMSR-E brightness temperatures for estimating sea ice concentration," *Monthly Weather Rev.* vol. 40, pp. 997–1013, 2012.
[31] H. Shi, B.-J. Sohn, G. Dybkjær, R. T. Tonboe, and S.-M. Lee, "Simultaneous estimation of wintertime sea ice thickness and snow depth from spaceborne freeboard measurements," *Cryosphere*, vol. 14, pp. 3761–3783, 2020.
[32] M. Shokr, "Field observations and model calculations of dielectric properties of Arctic sea ice in the microwave C-band," *IEEE Trans. Geosci. Remote Sens.*, vol. 36, no. 2, pp. 463–478, 1998.
[33] D. M. Smith, "Extraction of winter total sea-ice concentration in the Greenland and Barents Seas from SSM/I data," *Int. J. Remote Sens.*, vol. 17, pp. 2625–2646, 1996.
[34] G. Spreen, L. Kaleschke, and G. Heygster, "Sea ice remote sensing using AMSR-E 89 GHz channels," *J. Geophysical Res.*, vol. 113, 2008, Art. no. C0 2S03
[35] R. T. Tonboe and S. Andersen, "Modelled radiometer algorithm ice concentration sensitivity to emissivity variations of the Arctic sea ice snow cover," *Danish Meteorological Inst. Sci. Rep.*, pp. 04–03, 2004.
[36] R. T. Tonboe, G. Dybkjær, and J. L. Høyer, "Simulations of the snow covered sea ice surface temperature and microwave effective temperature," *Tellus A: Dynamic Meteorology and Oceanography*, vol. 63, no. 5, pp. 1028–1037, 2011.
[37] R. T. Tonboe *et al.*, "The EUMETSAT sea ice concentration climate data record," *Cryosphere*, vol. 10, pp. 2275–2290, 2016.
[38] R. T. Tonboe, H. Schyberg, E. Nielsen, K. R. Larsen, and F. T. Tveter, "The EUMETSAT OSI SAF near 50 GHz sea ice emissivity model," *Tellus Dyn. Meteorol. Oceanogr.*, vol. 65A, 2013, Art. no. 18380.
[39] R. T. Tonboe, "The simulated sea ice thermal microwave emission at window and sounding frequencies," *Tellus Dyn. Meteorol. Oceanogr.*, vol. 62A, pp. 333–344, 2010.
[40] S. M. Uppala *et al.*, "The ERA-40 Re-analysis," *Quart. J. R. Meteorol. Soc.*, vol. 131, pp. 2961–3012, 2005.
[41] F. J. Wentz and T. Meissner, "AMSR ocean algorithm, Version 2," *Tech. Proposal 121599A-1, Remote Sensing Systems*, Santa Rosa, CA, USA, 2000, p. 66.
[42] A. Wiesmann, and C. Mätzler, "Microwave emission model of layered snowpacks," *Remote Sens. Environ.*, vol. 70, no. 3, pp. 307–316, 1999.
[43] A. Wiesmann, C. Mätzler, and T. Weise, "Radiometric and structural measurements of snow samples," *Radio Sci.*, vol. 33, no. 2, pp. 273–289, 1998.

Rasmus T. Tonboe received the M.Sc. degree in geology from the University of Aarhus, Aarhus, Denmark, in 1997, and the Ph.D. degree in geophysics from the University of Copenhagen, Copenhagen, Denmark, in 2004.

He is currently an Associate Professor with the Technical University of Denmark in Copenhagen. He has field work experience, operating radiometers in the field, snow, and sea ice sampling, and installing meteorological monitoring stations on sea ice. His research interests include microwave and infrared remote sensing of sea ice in particular modeling of thermal emission and backscatter from sea ice and the use of forward model inversion for estimating sea ice snow cover, and other properties.

Dr. Tonboe is a member of ESA's MetOp SG MWI and ICI Science Advisory Group and the ESA CIMR Mission Advisory Group.

Vishnu Nandan received the Ph.D. degree in radar remote sensing of Arctic sea ice from the University of Calgary, Calgary, AB, Canada and the M.Sc. degree in earth observation sciences from ITC, Enschede, The Netherlands.

He was a Postdoctoral Researcher with the University of Victoria, Canada. He is currently a Research Associate with the University of Calgary and a Postdoctoral Researcher with the University of Manitoba, Winnipeg, MB, Canada. His research interests include polarimetric microwave remote sensing of sea ice, specialized in accounting snow and its geophysical properties affecting snow and sea ice parameter retrievals from radar satellites.

Marko Mäkynen (Member, IEEE) received the D.Sc. (Tech.) degree in electrical and communications engineering from the Helsinki University of Technology (HUT) (Aalto University since 2010), Espoo, Finland, in 2007.

From 1999 to 2006, he was a Senior Teaching Assistant with the Laboratory of Space Technology, Aalto University, where he was the Acting Director from 2007 to 2008. Has was Senior Scientist with the Marine Research Unit, Finnish Meteorological Institute, Helsinki, Finland, from 2009 to Jun 2021. Currently he is leading the Polar Oceanography and Sea Ice Research Group, Finnish Meteorological Institute, Helsinki, Finland. He is Docent in microwave remote sensing with Aalto University. His research interests include microwave and optical remote sensing of the Baltic and Arctic Sea ice and development of operational marine services.

Leif Toudal Pedersen (Member, IEEE) was born in Denmark in 1957. He received the M.S. degree in microwave engineering and the Ph.D. degree in passive microwave remote sensing of sea ice from the Technical University of Denmark (TUD), Kongens Lyngby, Denmark, in 1982 and 1992, respectively.

From 1982 to 2000, he was a Research Assistant with Electromagnetics Institute, TUD, and from 2000 to 2007, he was an Associate Professor with Oersted-DTU, Denmark. From 2007 to 2017, he was a Senior Researcher with Danish Meteorological Institute. Since 2017, he has been a part-time Senior Researcher with the Technical University of Denmark (DTU-Space) and part-time running his own company eolab.dk. His research interests include the retrieval of ice, ocean, and atmospheric parameters from multispectral microwave radiometer measurements as well as other methods for remote sensing of sea ice.

Dr. Pedersen has been a member of the Danish National Committee for Climate Research, the Danish National Committee for the International Polar Year, and the Danish National Committee for SCAR. He has also served as a Danish delegate to ESAs Programme Board for Earth Observations and has served on ESAs Sentinel-1 Mission Advisory Group.

Stefan Kern received the Diploma in meteorology from the University of Hannover, Hannover, Germany, in 1997, and the Ph.D. degree in physics from the University of Bremen, Bremen, Germany, in 2001.

Since 2001, he has been with the University of Hamburg, Hamburg, Germany, where until 2010, he worked on various aspects of sea-ice and ocean remote sensing with the Institute of Oceanography. Since 2010, he has been with Integrated Climate Data Center (ICDC), Center for Earth System Sciences and Sustainability (CEN), University of Hamburg. At ICDC, he has been responsible for satellite remote sensing data products across all spheres. He has continued working in the field of remote sensing of the marine cryosphere in both polar regions with a particular focus on product evaluation and uncertainty assessment—as for instance, in the framework of the ESA CCI sea ice project. His research interests include enhanced understanding and evaluation of the quality and limitations of satellite remote sensing products of the Earth.

Thomas Lavergne received the M.Sc. degree in applied mathematics and modeling from the National Institute of Applied Sciences (INSA), Toulouse, France, in 2003.

He was with the Joint Research Center of the European Commission (JRC), Ispra, Italy from 2003 to 2007. He is currently a Senior Research Scientist with the Norwegian Meteorological Institute, Oslo, Norway. He is the Principal Investigator for several climate and near-real-time products with the EUMETSAT Ocean and Sea Ice Satellite Application Facility (OSI SAF) and leads the ESA Climate Change Initiative (CCI) Sea Ice project. His research interests include remote sensing of sea ice, particularly from microwave radiometry.

Johanne Øelund received the B.Sc. degree in geophysics in 2013 and the M.Sc degree in geophysics, specializing in oceanography, in 2016 from the University of Copenhagen, Copenhagen, Denmark.

From 2020 to 2021, she was an Intern/Project Assistant with the Department of Management, Technical University of Denmark, Kongens Lyngby, Denmark, working with flooding and adaptation regarding climate change and extreme events. She is currently an academic employee with the Danish Meteorological Institute, Copenhagen, Denmark, working with mainly emissivity for the OSI-SAF project.

Gorm Dybkjær received the M.Sc. degree in physics from Roskilde University Center and University of Copenhagen, Copenhagen, Denmark, in 1994, where he received the Ph.D. degree in remote sensing and hydrology from the Institute of Geo-Science, in 2002.

He is currently a Senior Research Scientist with the Danish Meteorological Institute, Copenhagen, Denmark, where his scientific focus area is satellite remote sensing, with special interests in sea ice properties. Algorithm development, date analysis, validation, and calibration as well as development of remote sensing processors are main components of his work experience. His research interests include operational sea ice monitoring and development and analysis of climate data sets.

Roberto Saldo received the B.Sc. and M.Sc. degrees in electrical engineering from the Technical University of Denmark, Lyngby, Denmark, in 1994 and 1996, respectively.

He was a Research Assistant, from 1996 to 2007, with the Electromagnetics Institute, Technical University of Denmark, where he has been a Senior Research Engineer with the Division of Microwaves and Remote Sensing, Microwave and Remote Sensing Section, since 2007. He is part of the ESA Climate Change Initiative, Sea Ice Essential Climate Variable Validation Team and the Copernicus Climate Change Service and Sea Ice Thematic Assembly Centre. His research interests include producing reference validation data using synthetic aperture radar and passive microwave sensors.

Marcus Huntemann received the Diploma and Ph.D. degree in physics from the University of Bremen, Bremen, Germany in 2012 and 2015, respectively.

He has been with the Institute of Environmental Physics, University of Bremen, Bremen, Germany, since 2009. He was with the Alfred Wegener Institute of Polar and Marine Research from 2015 to 2020. He has participated in field work on snow and sea ice in the Arctic and Antarctic regions. His research interests include the modeling of microwave emission from sea ice and retrieval of geophysical parameters from microwave-based satellite sensors.